Frictional strength and fluidization of water-saturated kaolinite gouges at seismic slip velocities

Li-Wei Kuo [a,b,*], Wen-Jie Wu [a], Chia-Wei Kuo [c], Steven A.F. Smith [d], Wei-Ting Lin [a], Wei-Hsin Wu [a], Yi-Hung Huang [e]

[a] Department of Earth Sciences, National Central University, Taoyuan, Taiwan
[b] Earthquake-Disaster & Risk Evaluation and Management Center, National Central University, Taoyuan, Taiwan
[c] Center for Advanced Model Research Development and Applications, National Central University, Taoyuan, Taiwan
[d] Department of Geology, University of Otago, Dunedin, New Zealand
[e] Matsuki Hydraulic Industrial CO., Ltd., Taoyuan, Taiwan

ARTICLE INFO

ABSTRACT

Most previous experiments conducted on water-saturated clay-rich gouges sheared under extreme deformation conditions (including seismic slip rates e.g., 1 m/s, and displacements exceeding several meters) relied on gouge confinement using Polytetrafluoroethene (Teflon). Use of Teflon restricts such experiments to low normal stresses (≤ 2 MPa), which represents a significant limitation in our understanding of earthquake physics and seismic hazard assessment. To understand how normal stress and fluid affect the frictional behavior and deformation processes of clay-rich slipping zones, we performed rotary shear experiments using a purpose-built sample holder on water-saturated kaolinite gouges at a slip rate of 1 m/s and normal stresses ranging from 2 to 18 MPa. Results show that the apparent friction coefficient, μ, increases up to a peak value, μ_p, of ~ 0.17–0.46, associated with marked gouge compaction. This is followed by dramatic weakening with increasing displacement to a steady-state value, μ_{ss}, ~ 0.02–0.26 accompanied by gouge dilation. In-situ synchrotron X-ray diffraction and field-emission scanning electron microscopy show that clay aggregates within the gouge layer have a random fabric and do not experience mineral phase changes. On the basis of temperature measurements made during the experiments combined with a thermo-hydro-mechanical model, our results suggest that pore fluids within the gouge layer were mainly in liquid form during shearing. We conclude that dramatic weakening of kaolinite gouges at seismic rates under impermeable conditions is due to thermal pressurization, resulting in fluidization of the gouges. Our new experimental approach could be used to better understand earthquake physics and frictional processes of geological and civil interest.

1. Introduction

Catastrophic events such as earthquakes, tsunamis, and landslides are often associated with large coseismic slip localized to relatively thin fault and slip zones (Ma et al., 2006; Chester et al., 2013; Li et al., 2013). Therefore, understanding the strength and frictional behavior of slipping zones, and the associated deformation mechanisms, is crucial for earthquake physics and seismic hazard assessment (Scholz, 2000; Morre and Rymer, 2007; Collettini et al., 2009; Schleicher et al., 2010; Carpenter et al., 2011; Di Toro et al., 2011; Niemeijer et al., 2012).

At shallow crustal depths, water-saturated clay-rich gouges are common components of fault slipping zones (Chester et al., 1993; Caine et al., 1996; Vrolijk and van der Pluijm, 1999; Kuo et al., 2009; Si et al., 2014). The frictional properties of water-saturated clay-rich gouges have been experimentally investigated under a wide range of deformation conditions, including (1) slip rates of 1 μm/s to 1 mm/s and normal stresses ranging from 1 MPa to 200 MPa (Bos et al., 2000; Boulton et al., 2014; Brown et al., 2003; Carpenter et al., 2009, 2011, 2012; Chen et al., 2015; Faulkner et al., 2011; Ikari et al., 2009; Lockner et al., 2011; Logan and Rauenzahn, 1987; Morrow et al., 2000; Niemeijer and Collettini, 2014; Takahashi et al., 2007) and (2) intermediate (1 mm/s to 10 cm/s; Chen et al., 2017; Ferri et al., 2011; Lavallée et al., 2014; Yao et al., 2018) to high (10 cm/s to 10 m/s; Boulton et al., 2017; Chen et al., 2013; De Paola et al., 2011; Ferri et al., 2010, 2011; Lavallée et al., 2014; Ujiie

---

and Tsutsumi, 2010; Yao et al., 2018) slip rates and normal stresses ranging from 0.3 to 2 MPa (Fig. 1). Experimental studies of rock and gouge friction at intermediate to high slip rates have mainly been conducted with rotary shear-type experimental assemblies (e.g. Tsutsumi and Shimamoto, 1997).

In high-slip-rate rotary shear experiments, clay-rich gouges are typically contained in cylindrical or ring-shaped holders by Polytetra-fluoroethene (Teflon) sleeves, which have a very low friction coefficient when in contact with Teflon or other materials (e.g., Mizoguchi et al., 2007; references therein). However, gouge extrusion is difficult to prevent in high-velocity experiments, which often results in additional friction between the Teflon and other sample pieces (see the detailed discussion of Teflon sleeve in Sawai et al., 2012). For this reason, most of the rotary-shear friction experiments on water-saturated clay-rich gouges have been performed at relatively low normal stresses (≤2 MPa; Fig. 1a).

The addition of confining fluids to the gouge layer in the rotary shear configuration has represented a major challenge. Only a small number of rotary shear apparatus are capable of conducting experiments at

elevated temperatures in the presence of fluids, and at intermediate slip rates with relatively short displacements (e.g., <1 m; Niemeijer et al., 2008). Additionally, pore fluid pressures within gouge layers deformed at high-velocity are expected to transiently increase by shear-induced compaction (Faulkner et al., 2018), thermal pressurization (Faulkner et al., 2011), or thermochemical pressurization of water expelled from the crystal structure (Ferri et al., 2011). Rapid and extreme pressurization of pore fluid can result in decreasing contact between confining rings and other sample holder pieces, which facilitates gouge extrusion and a decrease of pore fluid pressures within the gouge layer. Because of the poor control on pore-fluid-pressures, most previous rotary shear experimental studies report the frictional strength of water-saturated gouges as the apparent friction coefficient (the ratio of measured shear stress over applied normal stress) (Yao et al., 2018; Rempe et al., 2020), which differs from the effective friction coefficient (the ratio of measured shear stress over effective normal stress (i.e., applied normal stress minus pore fluid pressure); Aretusini et al., 2021; Hunfeld et al., 2021) (Fig. 1b).

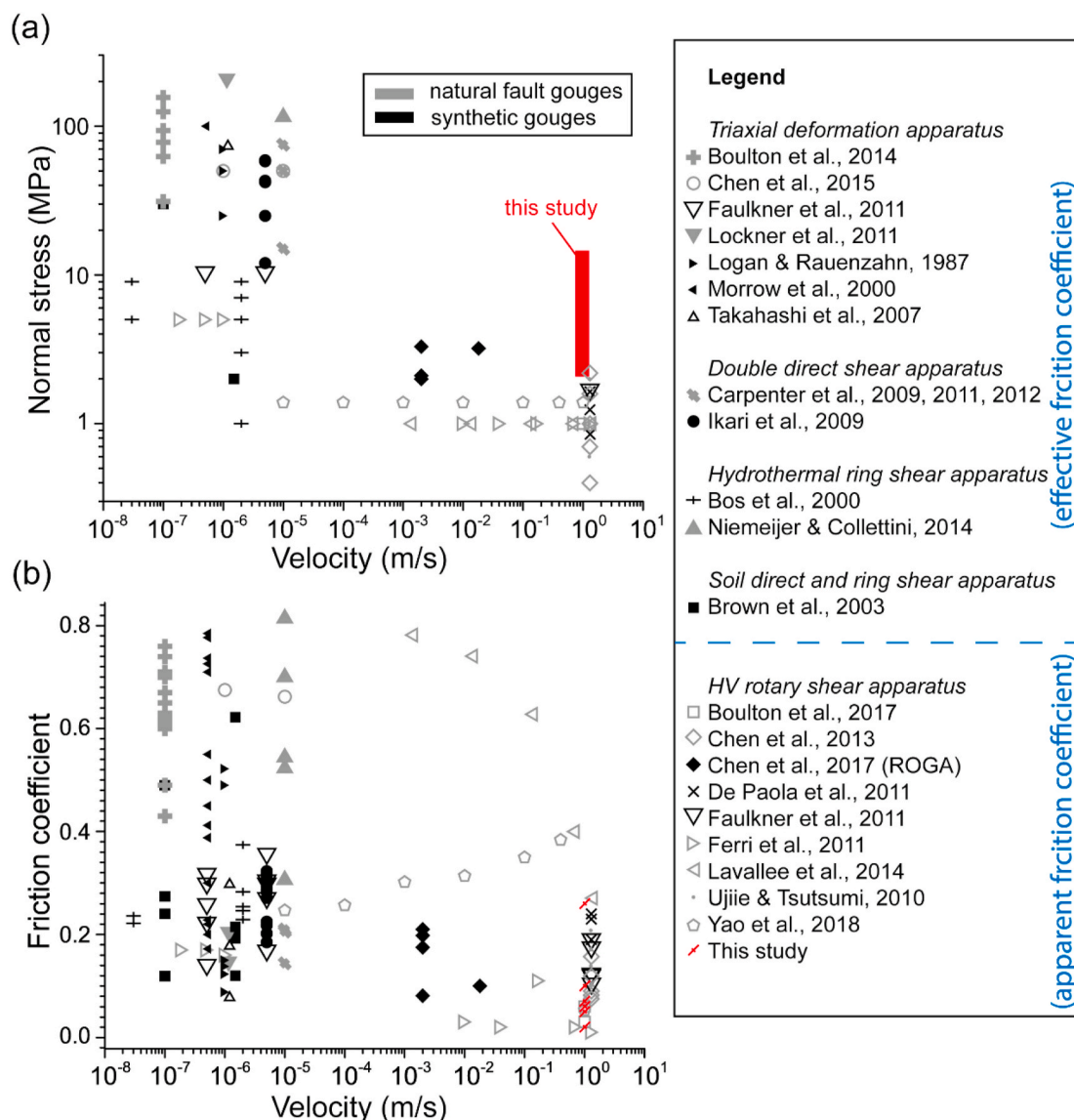In this paper, we performed rotary shear friction experiments on

Fig. 1. Summary of rock friction experiments conducted on water-saturated gouge materials. (a) Normal stresses and slip rates of reported rock friction experiments, and (b) the associated steady-state (apparent or effective) friction coefficient versus slip rates. Red area in (a) and the red symbols in (b) show the experimental conditions and the associated apparent friction coefficients, respectively, used in this study. (For interpretation of the references to color in this figure legend, the reader is referred to the Web version of this article.)

simulated fault gouges made of pure kaolinite using a purpose-built sample holder capable of reaching very high shear strains at high normal stresses (up to 18 MPa) and water-saturated conditions. Because pore fluid pressure could not be monitored or controlled, we report apparent friction coefficients and investigate transient mechanical and thermal pressurization processes using a thermo-hydro-mechanical model. We aim to investigate how normal stress and the presence of fluid affect the frictional behavior of a slipping zone, and to better understand the effects of thermal pressurization and gouge fluidization processes on the frictional behavior of pure kaolinite gouges at seismic slip rates under impermeable conditions. Our results may be applicable to frictional processes resulting in earthquakes or landslides because these commonly contain a considerable amount of clay minerals in their slipping zones (e.g., Kuo et al., 2009; 2011; Wu et al., 2005; 2017; Yang et al., 2014).
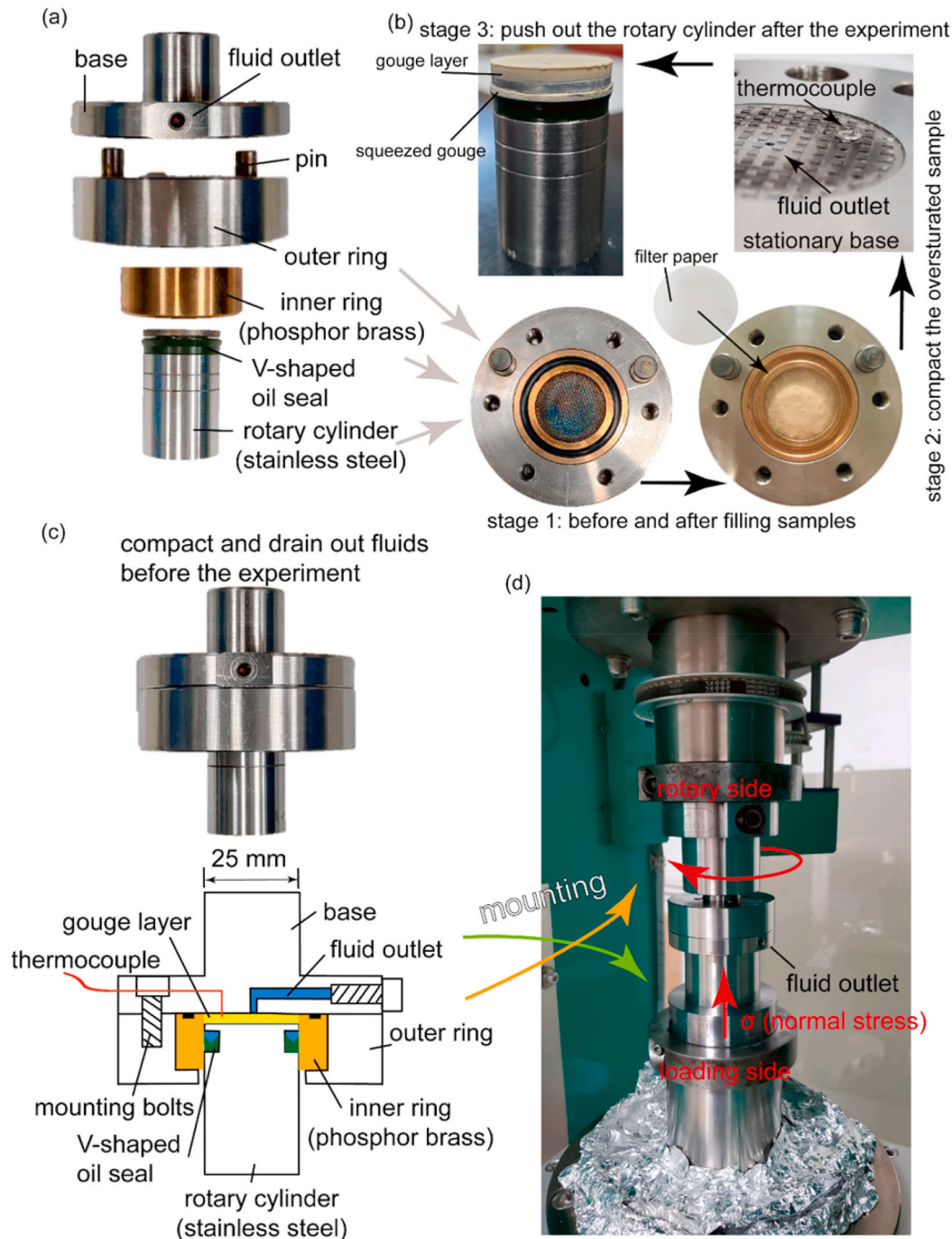

Fig. 2. The purpose-built sample holder and the low to high velocity rotary shear apparatus (LHVR) at NCU, Taiwan. (a) Photograph of the disassembled gouge holder. (b) Steps of sample preparation for the LHVR experiments. (c) Photograph and scale diagram of assembled gouge holder. (d) The LHVR equipped with the purpose-built sample holder.

2. Methods

2.1. Clay gouge sample holder and sample preparation

The sample holder was constructed to perform experiments on clay-rich gouges deformed under shallow crustal earthquake-like conditions: slip velocity of V ≥ 0.1 m/s and normal stresses of 2 ≤ σ < 20 MPa (Figs. 1a and 2). Clay-rich gouges are confined by a phosphor brass ring, a cylinder of stainless steel (rotary cylinder; 25 mm external diameter) and a stationary base of stainless steel (Fig. 2a). Rotary motion of the cylinder is driven by an axial locker connected to the rotary column of the low to high velocity rotary shear apparatus (LHVR). Normal load to the gouge layer is applied by the loading column of LHVR (Kuo et al., 2015).

The methods used to prevent gouge extrusion (or water leakage) and to obtain water-saturated conditions during the experiments are described in detail below. The stationary base and the cylinder are etched with a cross-hatch pattern to provide roughness at the boundaries of the gouge layer (Fig. 2b). The side wall of the cylinder is excavated to allow insertion of a V-shaped oil seal to confine water during the experiments (the green part of the rotary cylinder in Fig. 2a). There is 2 mm between the cross-hatch pattern on the rotary side and the excavation on the opposing side. Because air exists in the V-shaped space of the oil seal, water was piped into the V-shaped oil seal to expel air. The phosphor brass ring, the outer ring, and the cylinder of stainless steel (and other parts) are assembled before the wet clay samples are added (left portion of stage 1 in Fig. 2b). After adding the wet clay samples (right portion of stage 1 in Fig. 2b), we (1) cover the gouge layer with filter paper which allows for pore fluid drainage without gouge injection through the fluid outlet, (2) put the stationary base on the top of the sample holder, (3) mount the bolts to connect the stationary base and the outer ring, (4) confirm that air is expelled through the fluid outlet in the stationary base by manually compacting the cylinder and observing pore fluid drainage (Fig. 2b and c), and finally, (5) load the sample holder in to the LHVR (Fig. 2d).

The gouge samples are then compacted at the desired normal load for 30 min. During compaction, pore fluid can drain through the fluid outlet to the atmosphere or it can be compressed into the V-shaped oil seal (Fig. 2c). In the latter case, the V-shaped oil seal is expected to be pressurized by the fluids. The pressurized V-shaped oil seal prevents gouge extrusion when the cylinder rotates and slides over the ring-shaped phosphor brass during experiments, but also results in additional friction between the cylinder and the confined ring-shaped phosphor brass. Therefore, calibration tests using a gouge sample holder containing only water at various normal loads are required. After compaction of the gouge layer, the fluid outlet is closed. After the experiment, the V-shaped oil seal is not damaged or thermally decomposed.

2.2. Experimental procedures

We conducted experiments on 2 g of pure kaolinite with the LHVR installed at the National Central University (NCU), Taiwan. Because of the rotary configuration of the machine, both slip and slip rate increase towards the outer radius of the gouge layer. By following Hirose and Shimamoto (2005), we define the equivalent slip rate V_e:

$$V_e = \frac{4\pi R(r_{ext}^2 + r_{ext}r_{int} + r_{ext}^2)}{3(r_{ext} + r_{int})} \left[\frac{m}{s}\right] \tag{1}$$

where R is the revolution rate of the motor (i.e., the target R is 1149 rpm in this study), r_{ext} the external radius (12.5 mm), and r_{int} the internal radius (0 mm) of the samples (Fig. 2b). The aforementioned experimental conditions resulted in a target V_e of 1 m/s. Hereafter we refer to the "equivalent slip rate" as the slip rate. By assuming shear stress τ is nearly constant over the entire slip surface (Hirose and Shimamoto,

2005), the measured torque (M) is converted to the shear stress (τ):

$$M = \int_{r_{int}}^{r_{ext}} 2\pi\tau r^2 dr = \frac{2\pi\tau}{3}(r_{ext}^3 - r_{int}^3) \ [N \ m] \tag{2}$$

From Eq. (2), the apparent friction coefficient μ is shear stress τ versus normal stress σ:

$$\mu = \frac{\tau}{\sigma} = \frac{3M}{2\pi\sigma(r_{ext}^3 - r_{int}^3)} \tag{3}$$

The measured torque is the sum of the torque generated by deformation within the kaolinite gouge layer and the torque generated by friction due to contact between the cylinder (including the V-shaped oil seal) and the phosphor brass ring (referred to below as the intrinsic torque). In this study, we used calibration tests to determine the intrinsic torque and subtracted this from the total measured torque.

The experiments were conducted at normal stresses of 2, 5, 10, 15, and 18 MPa, at a target equivalent slip rate of 1 m/s and under water-saturated conditions. The acceleration and deceleration rates are 3.5 m/s². Mechanical data (torque, angular rotation, and axial displacement) were acquired at a frequency of 1 kHz. The initial gouge layer thickness was measured after compacting the gouge layer before the onset of shear. All experiments had an initial gouge layer thickness of 1.5 ± 0.2 mm prior to deformation. Because the state of the pore fluid within the gouge layer is crucial for recognizing its role in dynamic weakening, we conducted an additional experiment with a thermocouple to illustrate the temperature evolution with displacement. For this experiment, we drilled a hole at radial distance of ~8.3 mm from the center of the gouge layer (~two third of the radius of the gouge layer) and manually embedded a K-type sheath thermocouple (Ni–Cr thermocouple wires) into the stationary base. The tip of thermocouple was ~0.5 mm from one edge of the gouge layer and allowed for temperature to be estimated within the gouge layer during the experiment.

2.3. Microanalytical methods

After the experiments, the gouge layers deformed in wet conditions were poorly cohesive (shown as stage 3 in Fig. 2b). Therefore, we impregnated the gouge layers with an epoxy resin after the experimental products were dried in an environmental condition (at room temperature). We prepared petrographic thin sections and gouge layer slices ~1.5 mm thick which were cut perpendicular to the slipping surface for scanning electron microscopy. We used the field emission scanning electron microscope equipped with an energy dispersive spectrometer (FESEM/EDX; JSM-7000 F model) at the National Central University, Taiwan, to investigate the microstructures of the gouge layers. For SEM observations, both the petrographic sections and gouge slices were sputtered with a 10 nm thick platinum coat.

In addition, the gouge layer slices were also used for *in-situ* synchrotron X-ray diffraction (XRD). We utilized the synchrotron XRD installed at beamline BL01C2 in the National Synchrotron Radiation Research Center (NSRRC), Taiwan, to determine the mineral assemblages of the gouge layer before and after the LHVR experiments. The gouge layer slices were analyzed with X-rays at a wavelength of 0.774910 Å, with an electron beam energy of 1.5 GeV and a beam size of 100 μm diameter (e.g., Si et al., 2018; Hung et al., 2019; Wu et al., 2020).

3. Results

3.1. Starting materials

We used crystallized kaolinite particles (KA0001) received from Green Version Technology Ltd. as the starting materials. The liquid limit and plastic limit of kaolinite powder (CAS number: 1332-58-7) are 60 and 41, respectively (Alshibli and Akbas, 2007). The kaolinite (>90% in

volume) is < 14.65 μm in diameter with the mean diameter of 5.20 μm (Fig. 3), measured using a particle size laser diffraction analyzer (Beckman Coulter LS 13 320). The kaolinite (>90% in volume) after an experiment at 10 MPa (LHVR1223) is < 6.33 μm in diameter with the mean diameter of 2.70 μm (Fig. 3). This suggests that breakage of kaolinite grains occurred (i.e. smearing of kaolinite particles) during this large displacement experiment. Further details of the microstructure and mineralogy of kaolinite both in the starting materials and deformed samples are included below.

3.2. Calibration and limitation of the clay-gouge sample holder

To obtain the intrinsic torque of the sample holder (i.e., the friction derived from the contact between the cylinder (including the V-shaped oil seal) and the ring-shaped phosphor brass), we conducted a series of LHVR experiments using water only at a slip velocity of 1 m/s and a range of different normal stresses from 2 to 18 MPa (Fig. 4). All experiments and their corresponding conditions are listed in Table 1. During the experiments, no water leaks were observed.

The intrinsic torque evolves with displacement and varies slightly depending on the normal load (Fig. 4a), but overall, the strength trend is similar at different normal loads (Fig. 4b). Between 2 and 18 MPa normal stress, the measured torque initially increases to a peak value of ~1.95–3.14 Nm and then decreases with displacement to reach a steady-state value of ~1.35–1.85 Nm (Fig. 4a). We plot the measured peak and steady-state torques as a function of normal stress (Fig. 4b). This shows that the peak torque depends weakly on the applied normal stress. In contrast, the steady-state torque shows a relatively constant value and is independent of normal stress. There is constant dilation with increasing displacement (a total of ~0.1 mm of dilation after 20 m slip) which is independent of normal stress (Fig. 4a).

The metal sample holder contains almost constant intrinsic steady-state frictional resistance (the torque from the contact between metal and the V-shaped oil seal) from 2 to 18 MPa (Fig. 4). The presence of extruded gouge particles at the edge of the layer (Fig. 2b) likely results in additional shear resistance during sliding. The combination of intrinsic torque and the extruded gouge will contribute significantly to the

measured torque if experiments are performed at low normal stresses (e. g., 2 MPa). Therefore, the gouge sample holder was designed for gouge materials deformed at normal stresses ≥2 MPa. The conditions used in previous rotary or ring shear apparatuses are listed for comparison with the new sample holder in Table 2.

3.3. Correction of the mechanical data of clay-gouge sample holder

Fig. 5a shows the torque before and after the correction to account for the intrinsic torque of the sample holder in experiment LHVR1215 (water-saturated kaolinite gouge, 1 m/s, 15 MPa). A comparison of the calibration test with the measured torque in experiment LHVR 1215 (Fig. 5a) shows that the contribution to torque from the sample holder in this experiment was equivalent to ~33% of the measured torque during steady-state sliding. Because the intrinsic torque of the sample holder is similar at all measured normal stresses (2–18 MPa; Fig. 4), this indicates that the contribution to torque from the sample holder will increase at lower normal stresses. In this study, we report mechanical data following a correction to account for the torque contribution from the sample holder. For each experiment, we corrected the measured torque values by subtracting the intrinsic torque of the gouge sample holder at the same normal stress. A summary of the experimental conditions and the mechanical data from the calibration tests is shown in Table 1.

We use the empirical equations of Hirose and Shimamoto (2005) and Mizoguchi et al. (2007) to fit the slip-weakening behavior observed in the experiments (example of LHVR 1215 at 15 MPa shown in Fig. 5b). Three key parameters are: the peak friction μ_p, the steady-state friction μ_{ss}, and the critical slip weakening distance D_c:

$$\mu = \mu_{ss} + (\mu_p - \mu_{ss})e^{\ln(0.05)d/D_c} \qquad (4)$$

In fitting equation (4), values of μ_p and μ_{ss} were manually determined. μ_P in experiment LHVR 1215 was at a displacement of ~1 m, and D_c was determined using equation (4). The parameter D_c is defined as the slip distance needed to achieve 95% of the total weakening towards steady-state friction, and is often interpreted as the distance needed for the slipping zone to weaken during an earthquake (Hirose and Shimamoto, 2005).

3.4. Mechanical data from deformed kaolinite gouge layers

The apparent friction coefficient, μ, evolves with displacement and varies as a function of normal stress (Fig. 6a). μ increases to a peak value μ_p of ~0.17–0.46 and then dramatically decreases to a lower steady-state value of ~0.02–0.26 (an average value during the steady-state sliding). Regarding the entire experimental dataset, the peak shear stress τ_p and steady-state shear stress τ_{ss} increase linearly with normal stress, resulting in an apparent friction coefficient of ~0.15 and ~0.05 for μ_p and μ_{ss}, respectively (Fig. 6b). Because our samples are initially noncohesive, the relatively small cohesive terms can be attributed to the presence of the V-shaped oil seal (Fig. 4a) or to weak Van der Waals or hydrogen bonds between clay particles (Brantut et al., 2008).

The axial displacement, ε, evolves with slip and varies at different normal loads. During the initial 1.5 m of displacement, the gouge layers compact ~0.10–0.18 mm due to shear-induced compaction of the clay particles. After 1.5 m of displacement, the gouge layer gradually dilates until the end of sliding. Following initial compaction, the gouge layers dilate by ~0.14 (LHVR1216) to ~0.61 mm (LHVR1214). Our experiments show that the onset of dilation corresponds to the initiation of slip weakening (Fig. 6a). Mechanical work rate (power density; $\Phi = \tau V$) is a key parameter controlling the rate of temperature increase in the slipping zone, which can trigger mechanically and thermally activated weakening processes (Di Toro et al., 2011). Therefore, we plot the total dilation (i.e. following initial compaction) of the gouge layers as a function of the calculated power density ($\tau_{ss} V_e$) in Fig. 7. The total dilation increases linearly with increasing power density (Fig. 7).
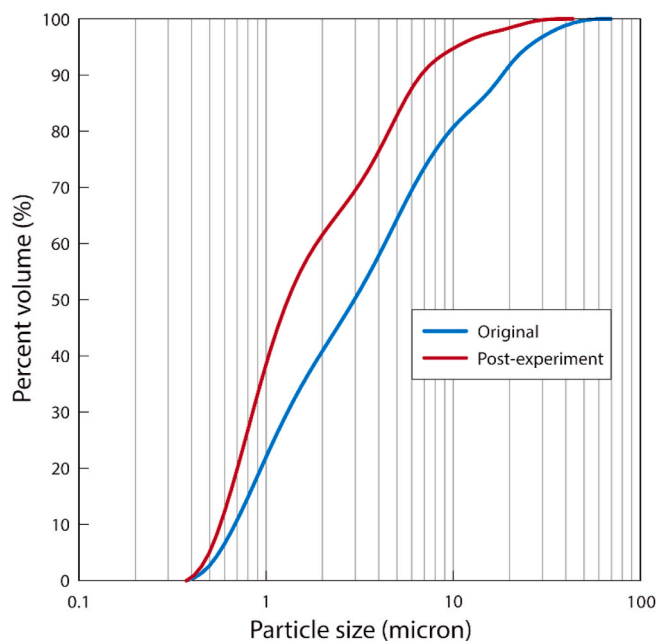

Fig. 3. Cumulative grain size distributions of the tested kaolinite samples before and after experiments (deformed at 10 MPa; LHVR1223) determined with a commercial laser diffraction particle size analyzer (Beckman Coulter LS 13 320).
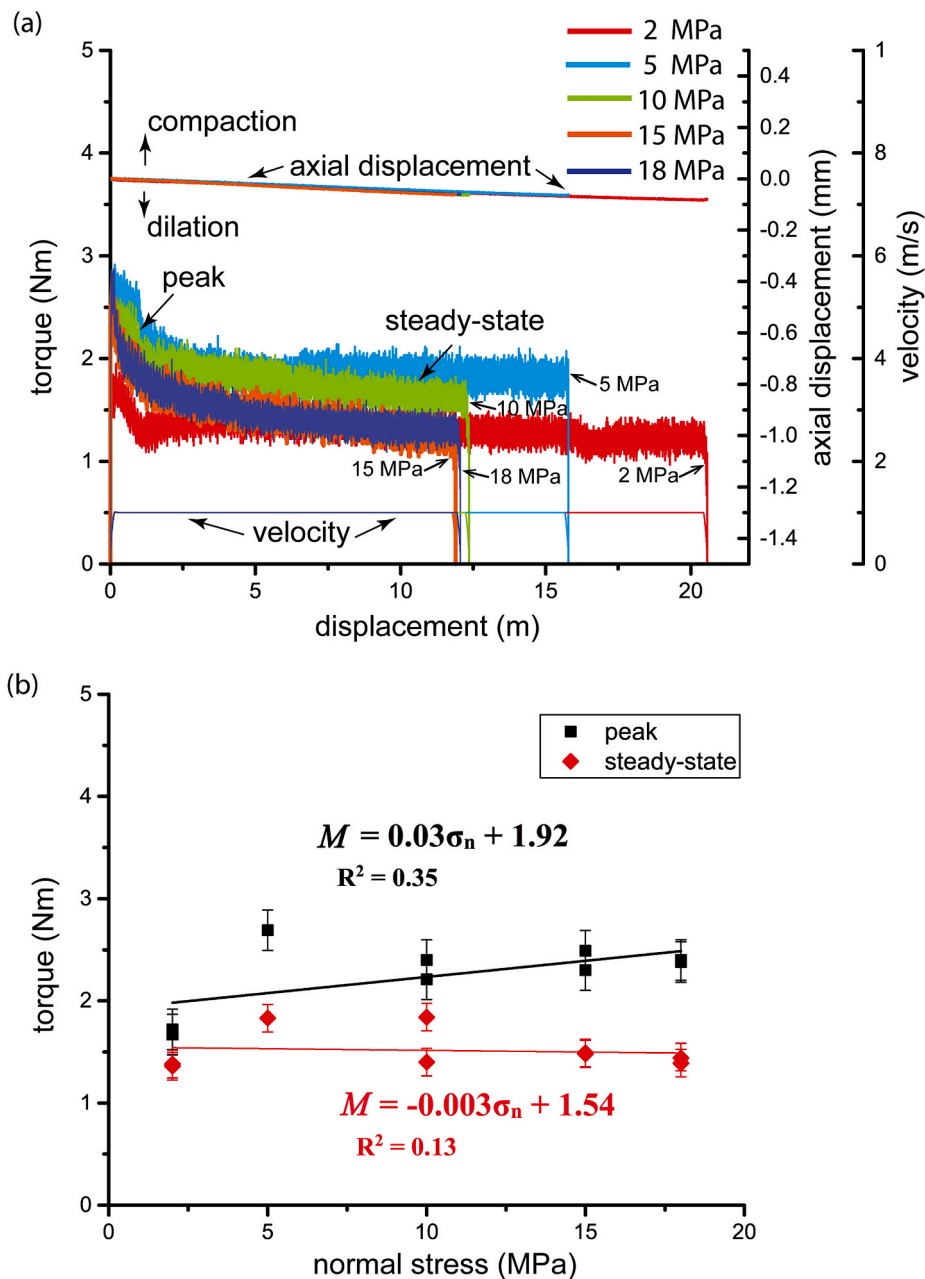
Fig. 4. Intrinsic shear resistance of the sample holder (water inside only). (a) Measured torque, axial displacement, and velocity versus displacement at different normal stresses. (b) Measured torque versus normal stress obtained at peak and steady state from experiments deformed at 1 m/s.

In addition, by fitting our mechanical data with Equation (4), we obtain the critical slip weakening distance, D_c, which ranges from ~1.15 to ~4.23 m. Fig. 8 shows D_c plotted as a function of normal stress, together with a summary of previous studies conducted on dry and saturated clay-rich gouges (Boulton et al., 2017; De Paola et al., 2011; Ferri et al., 2011; Chen et al., 2013, 2017; Togo et al., 2011, 2016). Fig. 8 shows that at normal stresses >2 MPa, D_c of dry and wet clay gouges is independent of the applied normal stress. In addition, D_c of dry and wet clay gouges at normal stresses <2 MPa is longer than the one from normal stresses >2 MPa.

3.5. Mineralogy of starting materials and deformed gouges

Mineralogical phase changes are most likely to be detected around the external edge of the gouge layer because of the highest rotational velocity and temperature rise experienced there. Mineralogical phases were determined through successive XRD analyses of thin sections cut perpendicular to the slipping surface (Fig. 9a). No mineral phase changes were observed in the XRD data, regardless of the applied normal stresses or the position within the gouge layer (Fig. 9b). The results indicate that all of the deformed gouge layers contain only the typical crystal structure of kaolinite, identical to the starting materials (Fig. 9b).

3.6. Microstructural observations

Microstructures were observed in radially cut thin sections (Fig. 9b) through the cylindrical gouge layers. As microstructural observation was conducted using radial thin sections perpendicular to the shear direction, shear-related structures such as Riedel shear and foliated zone may not be observable. We conducted one compaction experiment at a normal stress of 18 MPa for comparison with deformed gouges. We show representative SEM and back-scattering electron images of products

Table 1

List of experiments, conditions, and mechanical data, including the critical slip weakening distance D$_c$. All listed experiments were conducted at a slip rate of 1 m/s under water-saturated conditions.

number	Normal stress (MPa)	Total displacement (m)	Peak torque (Nm)	Steady-state torque (Nm)	Corrected peak shear stress (MPa)	Corrected steady-state shear stress (MPa)	Corrected peak friction	Corrected steady-state friction	D$_c$ (m)
LHVR1999-1 (only water)	2	20.50	2.01	1.36	N/A	N/A	N/A	N/A	N/A
LHVR1999-2 (only water)	5	15.78	2.91	1.85					
LHVR1999-3 (only water)	10	12.36	2.62	1.76					
LHVR1999-4 (only water)	15	11.90	2.79	1.43					
LHVR1999-5 (only water)	18	12.06	2.87	1.41					
LHVR1999-6 (only water)	18	15.56	3.12	1.35					
LHVR1999-7 (only water)	15	15.52	3.15	1.46					
LHVR1999-8 (only water)	10	15.33	2.68	1.39					
LHVR1999-10 (only water)	2	20.56	1.95	1.38					
LHVR1213	2	13.79	4.86	3.52	0.91	0.52	0.46	0.26	1.55
LHVR1214	18	8.12	15.37	6.42	3.23	1.23	0.18	0.07	2.26
LHVR1215	15	10.73	12.26	5.32	2.57	0.95	0.17	0.06	2.51
LHVR1216	5	10.69	6.31	2.96	1.03	0.27	0.21	0.05	2.35
LHVR1217	10	12.01	9.46	4.65	1.79	0.71	0.18	0.07	1.82
LHVR1223	10	10.26	14.11	5.90	2.89	1.01	0.29	0.10	1.15
LHVR1230	5	12.31	8.22	3.10	1.39	0.30	0.28	0.06	1.92
LHVR1232	2	11.73	3.90	1.56	0.63	0.04	0.31	0.02	4.23
LHVR1291	15	9.72	14.07	4.33	2.93	0.71	0.20	0.05	1.38
LHVR1292	18	7.42	15.30	5.65	3.17	1.04	0.18	0.06	2.99
LHVR1614	2	11.38	5.02	2.64	0.82	0.31	0.41	0.15	7.06
LHVR1615	2	10.45	4.96	2.79	0.90	0.34	0.45	0.17	4.14

Note1: steady-state parameter is averaged from 5 m to 7 m (total slip is 7.42) in LHVR1292 (others are averaged from 5 to 7.5 m).

Table 2

Features of other rotary-shear or ring-shear apparatus, compared with the new sample holder presented in this paper.

	Sassa et al. (2014)	Tomasetta et al. (2013)	Lin et al. (2018)	Smith et al. (2013)	Niemeijer et al. (2008)	Yao et al. (2018)	This study
Apparatus	ICL-2	HT-ASC		SHIVA	hydrothermal ring shear	Rotary shear	LHVR
Inner dia. (mm)	100	60	110	35	22	25	0
Outer dia. (mm)	142	118	149	55	28	40	25
Max. normal stress (MPa)	3	0.055	2.71	25	600 (Pp: 300)	1.3	18
Maxi. Slip speed (m/s)	0.5	5*10E-4	3*10E-5	3.2	3*10E-6	2.6	1.3
Undrained condition	Yes	No	Yes	No	Yes	Yes	Yes
Pore-pressure controlled	Yes	No	Yes	No	Yes	Yes	No
Pore-pressure monitoring	Yes	No	Yes	No	Yes	No	No
Temperature monitoring	No	Yes	No	No	Yes	No	Yes
Displacement	no limit	no limit	no limit	no limit	up to 100 mm	no limit	no limit

derived from the compaction experiment (Fig. 10a and b), and shear experiments performed at 2 (Fig. 10c and d), 10 (Fig. 10e and f), and 18 MPa (Fig. 10g and h). The kaolinite had a light cream color before the experiments. The compacted gouge layer shows a homogenous microstructure consisting of aggregates of sub-rounded kaolinite particles <1 μm in size (Fig. 10a and b). After the experiments, the deformation within the gouge layer is weak: a distinct color variation was absent, and (assumed) slipping zones (close to the rotary part of the cylinder) were observed consisting of randomly oriented smeared kaolinite particles (Figs. 9a and 10c-h). Close to the stationary side, the kaolinite particles after the experiments exhibited somehow flaking but had a similar size and sub-rounded shape as the starting materials. Overall, the gouge layers are characterized by a random distribution of kaolinite particles, regardless of the radial position within the gouge layer and the applied normal stress (Fig. 10c–h). Some open fractures formed parallel to the gouge layer margins, but we could not distinguish between dilation-related opening during the experiments and opening due to unloading at the end of the experiment.

4. Discussion

4.1. Frictional strength of water-saturated kaolinite gouges

At a normal stress of 2 MPa, the contribution of torque from the sample holder to the measured torque ranges from 40% to 52% (Table 1). Therefore, before further interpreting the mechanical data from higher normal stresses (5–18 MPa), we compare our data at 2 MPa to previous results. In general, the frictional strength of kaolinite at 2 MPa in our experiments is consistent with previous experiments performed on water-saturated clay-rich gouges (Fig. 1). The apparent friction coefficient for saturated kaolinite in our experiments is $\mu_p = \sim 0.31$–0.46 and $\mu_{ss} = \sim 0.02$–0.26 (Fig. 6; Table 1), which is comparable to $\mu_p = \sim 0.33$ and $\mu_{ss} = \sim 0.12$ in Ujiie et al. (2011), $\mu_p = \sim 0.16$–0.67 and $\mu_{ss} = \sim 0.03$–0.14 in Boulton et al. (2017), and $\mu_p = \sim 0.10$–0.19 and $\mu_{ss} = \sim 0.01$–0.05 in Ferri et al. (2011) (all conducted on water-saturated clay-rich gouges at normal stresses $\leq$ 2 MPa). We also note several other similarities between our results and these previous studies, including:
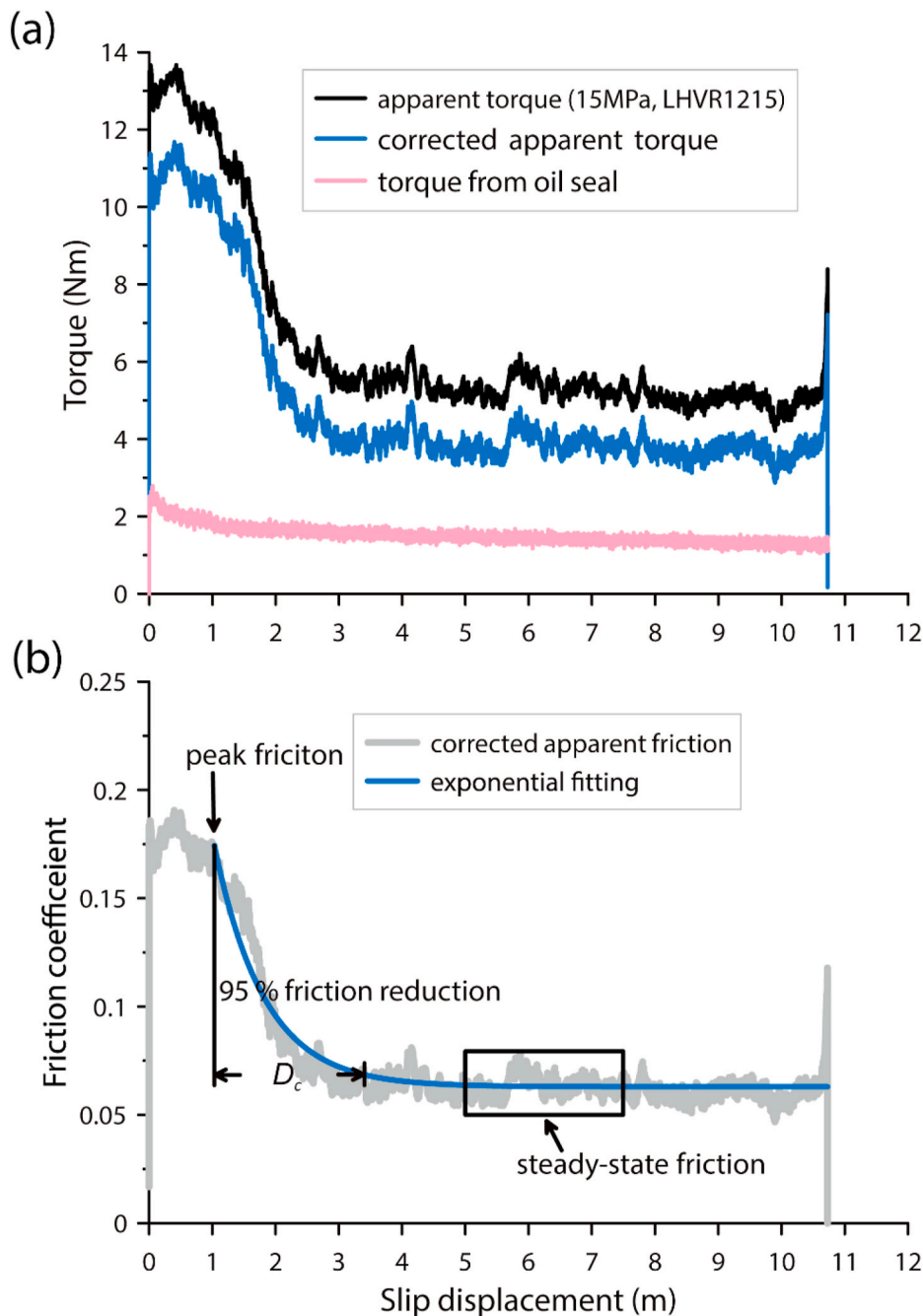
Fig. 5. Correction of torque of water-saturated kaolinite samples and the fitting of frictional strength for D_c. (a) Measured torque (and corrected torque by subtracting the torque from V-shaped oil seal) versus displacement at a normal stress of 15 MPa and slip rate of 1 m/s. (b) Corrected frictional coefficient versus displacement at a normal stress of 15 MPa. Blue line showing the least-squares fit to the data with Equation (4) and the estimated D_c. (For interpretation of the references to color in this figure legend, the reader is referred to the Web version of this article.)

(1) a similar frictional evolution (e.g., our Figs. 6 and 4 in Boulton et al., 2017); (2) similar trends of compaction and dilation in wet gouges (e.g., our Figs. 6 and 5 in Ujiie et al., 2011); and (3) the lack of grain comminution in wet gouges (e.g., our Figs. 10 and 15 in Ujiie et al., 2011).

The most significant mechanical response of the wet gouge layers at higher normal stresses (5–18 MPa) is a significant decrease in the friction coefficient from a peak of ~0.17–0.29 to a steady-state ~0.05–0.10. The relatively high steady-state friction coefficient of 0.26 measured at 2 MPa normal stress (Fig. 6) implies that experiments performed at relatively low normal stresses (<5 MPa) may not be representative of the frictional properties of wet kaolinite gouges at crustal depths (e.g., >100 m). These findings are in agreement with preliminary observation from room humidity friction experiments performed on gouges rich in carbonaceous-materials at 5–25 MPa (Kuo et al., 2014b).

4.2. Evolution of pore pressure and temperature within the gouge layer

To further understand the temperature evolution with displacement at deformation conditions identical to experiment LHVR1217 (10 MPa; Fig. 11), we conducted an experiment (LHVR1223) with *in situ* temperature measurement by inserting a K-type sheath thermocouple through the stationary base piece and into approximately the middle of the gouge layer (Fig. 2b). The temperature of the gouge layer gradually increased to ~140 °C after ca. 4 m of slip (Fig. 12c), then increased more slowly to a final value of ~160 °C at the end of the experiment (10.25 m of slip). The measured temperature only reflects the bulk temperature of the gouge layer, and it is possible that the local temperature at active asperities could be higher due to flash heating.

In order to investigate the weakening mechanisms operating during the experiments, information on pore fluid pressure and temperature
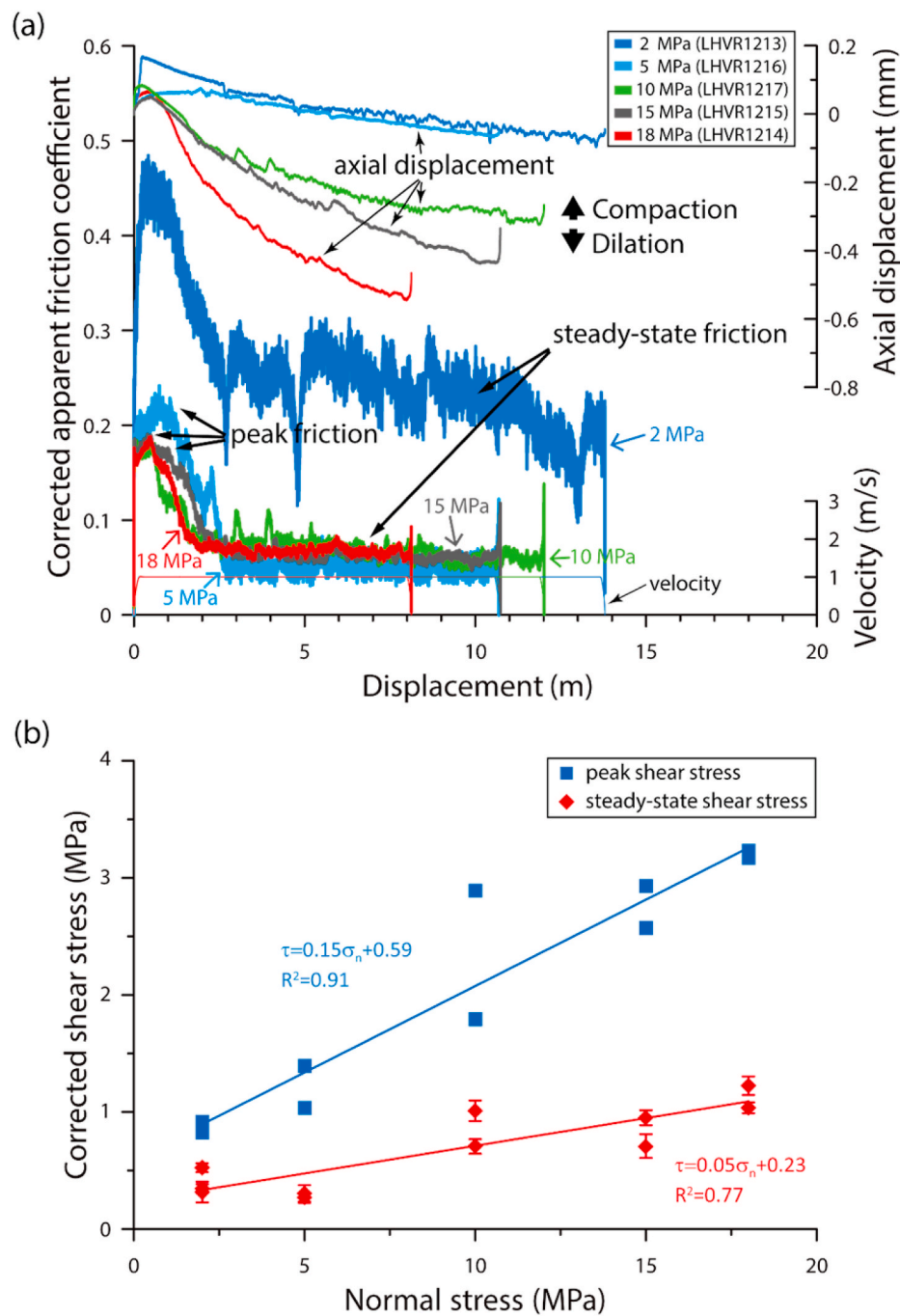
Fig. 6. Frictional strength at 1 m/s of water-saturated kaolinite samples. (a) corrected apparent friction coefficient (corrected shear stress/normal stress) versus displacement for five experiments (LHVR1213 to LHVR1217) carried out at normal stresses of 2–18 MPa. (b) corrected shear stress versus normal stress at peak and steady state for all experiments at 1 m/s.

within the gouge layer is required. An increase of pore pressure is expected in the slipping zone within the gouge layer, where is commonly close to rotary side of the apparatus. Therefore, direct measurement of pore pressure close to the slipping zone of gouge layer is challenging when the experiments are conducted at seismic rates (Aretusini et al., 2021). As a first-order approximation, we developed a thermo-hydro-mechanical (THM) model to estimate the local pressure-temperature conditions inside the gouge layer during sliding. We utilized the computer program HYDROGEOCHEM 4.3 to develop a 2D axisymmetric finite element model, which provides a coupled model of water flow (H), thermal transport (T), solute transport (C), geochemical kinetic/equilibrium reactions (R), and geomechanics (M)

in saturated-unsaturated porous media in two dimensions (Yeh, 1999, 2000; Yeh et al., 2017).

The geometry, mesh, material parameters, and heat sources are shown in Fig. 11. The thickness of the gouge layer is 2 mm. The total node and triangular element numbers are 1597 and 3108, respectively. Four different material types were incorporated in to the model: stainless steel, fault gouge, oil seal, and brass sleeve. The key flow, thermal, and mechanical parameters used in the model are listed in Table 3. The specific heat of water is 4202 J/(kg·K) and the thermal expansion coefficient of water is 2.1 E-41/K. We used a single phase of water in the modeling (i.e., water cannot be vaporized during the modeling). In addition, the hydraulic conductivity of the gouge was assumed to be
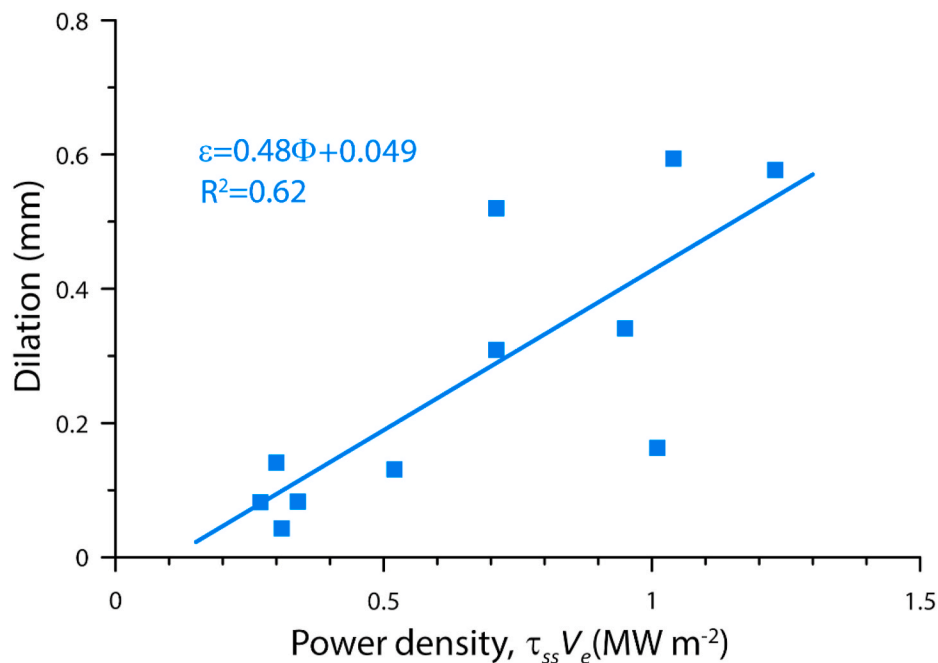
Fig. 7. Dilation (the increase of gouge layer) versus power density (shear stress times velocity).

1.6E-13 m/s, and the total porosity of the gouge was assumed to be 30% (e.g., Bossart, 2005). Because the metal pieces (stainless steel and brass) and the V-shaped oil seal are impermeable, we set the hydraulic conductivity of these model domains with extremely low values (seven to ten orders of magnitude lower than the hydraulic conductivity of fault gouge).

There are two heat sources considered in the numerical model; one is located at the interface between the rotating cylinder and the gouge layer (heat source 1), and the other is located at the interface between the V-shaped oil seal and the brass sleeve (heat source 2; Fig. 11b). Heat from those sources was calculated from the measured shear stresses of both the gouge layer and the V-shaped oil seal, respectively. The frictional work was calculated as shear stress (τ) multiplied by the slip rate (V) at a radial position (r) as follows:

$$Q(t,r) = \tau(t)V(r,t) \tag{5}$$

Total frictional work during an experiment can be distributed between frictional heating, chemical reactions, phase transitions, grain deformation, and comminution (Rice, 2006). On the basis of our observations (Figs. 9 and 10), only the first process is considered in our modeling because there is no evidence for significant changes to the grain size or mineralogy in the deformed gouge layers. All frictional work was thus assumed to be converted into heat during slip. The initial temperature and pore fluid pressure are set as 25 °C and 1 atm, respectively. For the flow and thermal modules, we used a no flux condition at the outer boundary. Finally, for the geomechanics module, the roller boundary was set at the bottom boundary and the symmetry axis. Normal stress was set to 10 MPa on the top of the gouge layer.

In a rotary shear configuration, based on the assumption of a spatially uniform friction coefficient in the slipping zone, 87.5% of the measured torque is derived from the friction in the outer half of the gouge layer (Yao et al., 2013). This suggests that thermally activated deformation processes are more likely to be significant in the outer half of the cylindrical layer. Therefore, we report the calculated temperature and pore fluid pressure evolution at a radial distance of 8.33 mm from the center of the gouge cylinder, which is also the position of the inserted thermocouple in experiment LHVR1223 (Fig. 12).

Our modeling indicates that experiment LHVR1223 attained a maximum temperature of ~366.85 °C and a maximum pore fluid

pressure of ~9.28 MPa along the outer edge of the gouge layer (Fig. 12a and b). At the position of the thermocouple (8.33 mm from the center of the gouge cylinder), the modeled temperature increases to ~105 °C after < 4 m of slip, and continues to rise gradually during steady-state sliding, reaching a value of ~156 °C by the end of the experiment (Fig. 12c). The modeled temperature is very similar to the temperature measured in the same position using the thermocouple (Fig. 12c). Our model likely overestimates the maximum temperatures because we did not consider the latent heat associated with the liquid-vapor transition (Chen et al., 2017).

The modeled pore fluid pressure rapidly increases to ~3.61 MPa after <0.2 m of slip, and then gradually reaches a value of ~4.17 MPa after 1 m of slip, before decreasing slightly to a final value of 4.09 MPa by the end of the experiment (Fig. 12c). The rapid increase of modeled pore fluid pressure correlates with the measured compaction at the initiation of sliding (Fig. 6a), suggesting that shear-induced compaction may cause a rapid increase of pore fluid pressure. In addition, a gradual decrease of pore fluid pressure is consistent with the observed constant dilation measured in the gouge layer, suggesting that shear-induced dilatancy correlates with a pore pressure drop. Our results are consistent with the recently reported data by Hunfeld et al. (2021) which is also conducted high-velocity experiments on water-saturated gouges at normal stresses of 2.5–20 MPa.

4.3. Potential weakening mechanisms in water-saturated kaolinite gouges

Overpressure of water due to gouge compaction can be likely neglected because of free path of fluid drainage to atmosphere during lasting long-term compaction. During the experiments, the local pressure-temperature conditions within the gouge layers can vary significantly, and a phase change from liquid water to vapor gas is likely. Dynamic weakening could involve fluidization of gouge due to water vaporization (Chen et al., 2017a, b), thermal pressurization (Brantut et al., 2008; Chen et al., 2013; Hunfeld et al., 2021), and thermo-chemical pressurization (Brantut et al., 2010; De Paola et al., 2011). The latter process can likely be excluded because of the lack of mineralogical phase changes observed within the deformed gouge layers (Fig. 9).

Four lines of evidence support that the interpretation that kaolinite gouge layers were fluidized due to thermal pressurization: (1) The lack
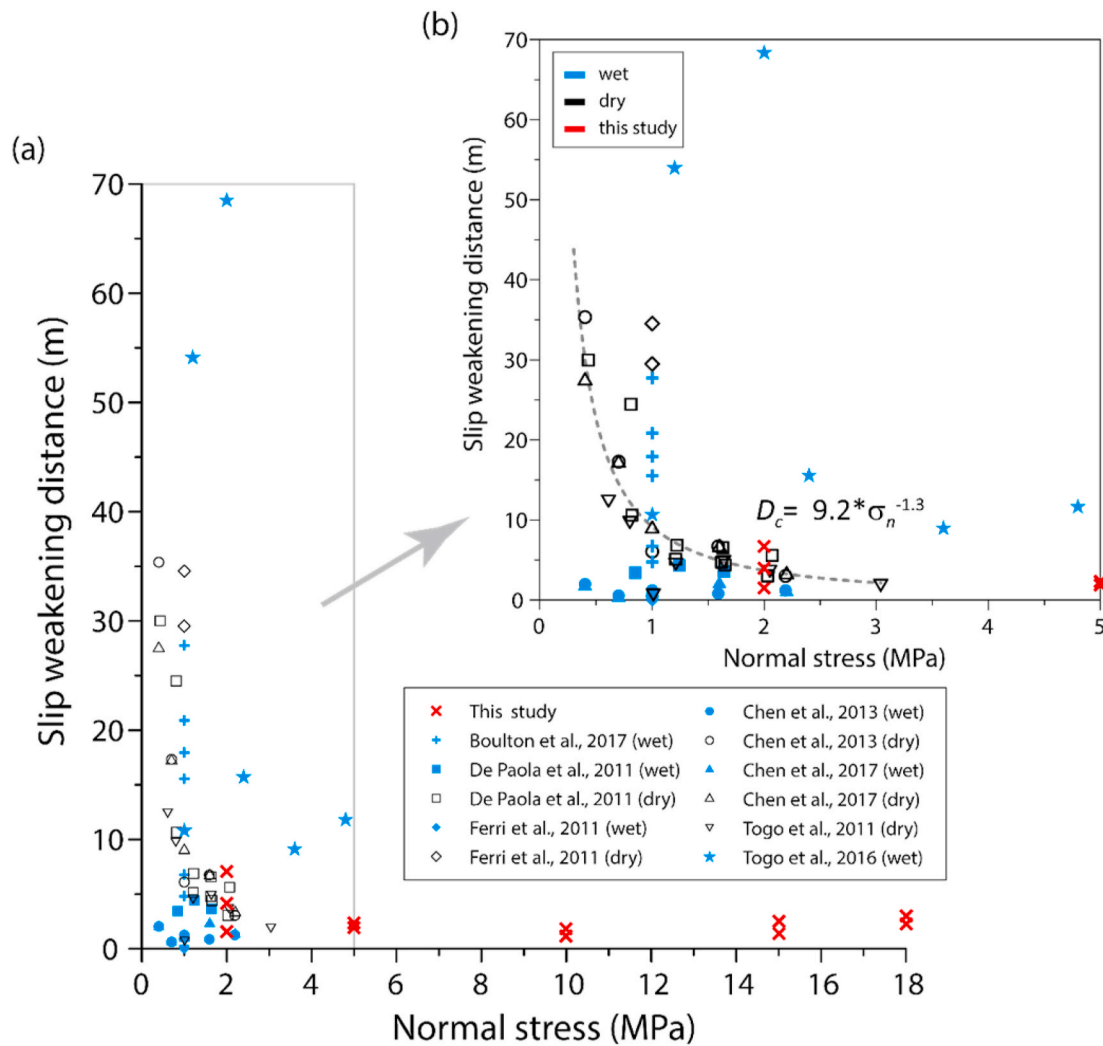
Fig. 8. Slip-weakening distance D_c versus normal stress in experiments performed on dry and wet gouge samples. (a) D_c versus normal stress up to 18 MPa. (b) Enlarged section of D_c versus normal stress.

of stain localization and the random fabric of smeared kaolinite particles after the experiments (Fig. 10; Boulton et al., 2017; Kitajima et al., 2010; Ujiie et al., 2011). (2) The modeled and measured temperatures (<370 °C), together with the lack of phase changes, suggest that frictional heating was insufficient to trigger processes such as frictional melting (Spray, 2005; Di Toro et al., 2006), and thermal decomposition or dehydroxylation of clay minerals (Han et al., 2007; Collettini et al., 2013; Ujiie et al., 2011) (Figs. 9 and 12). This is consistent with previous studies showing that thermal pressurization maintains sliding at relatively low temperatures (e.g., Acosta et al., 2018). (3) The axial dilation of the gouge layers is proportional to the power density (Fig. 7), consistent with the assertion that the power density is correlated with thermal expansion of the pore fluid within the gouge layer. Thermal expansion of pore fluid gradually increases with cumulative slip (Figs. 6a and 12c), suggesting that thermal pressurization allows clay particles to rotate and move in suspension with a mean free path larger than the grain size. Finally, (4) Based on the pressure-temperature conditions of the water phase diagram (Chen et al., 2017b; Weatherley and Henley, 2013), the temperatures for water vaporization at 3.61–4.17 MPa (experiment LHVR1223; Fig. 12) are estimated as ~244–252 °C. The modeled and measured bulk temperatures in this experiment are far below the temperatures required for vaporization, suggesting the pore fluids remained mainly in liquid form. In addition, our modeling suggests that pore pressure initially rises much faster than

temperature such that the pore fluid cannot vaporize before entering a supercritical phase, suggesting that vaporization can be inhibited by the thermal pressurization in low permeability gouges (Chen et al., 2017b). Due to the complete sealing provided by the gouge sample holder (Fig. 2), water cannot be expelled and drained from the slipping zone during shear deformation. This suggests that pore pressure derived from thermal pressurization could be sustained within the gouge layer during shear deformation, resulting in a decrease of effective normal stress and the associated weakening behavior (Fig. 12; Hunfeld et al., 2021).

Water vaporization may locally occur in the gouges because a temperature of ~370 °C along the outer edge of the layer would allow pore fluids at a local pore pressure of ~9.28 MPa to vaporize (Fig. 12). Additionally, a drop in fluid pressure due to progressive dilation could trigger a phase change to vapor. Water vaporization is predicted to result in both significant pressurization and dramatic dilation of the gouge layer, because the density of vapor water can be three orders of magnitude lower than that of liquid water in the same conditions (Chen et al., 2017b). The phase change of water would result in the various compressibility of water and the associated the specific storage within the gouge layer, which is required to be considered for the modeling. Here, the lack of dramatic dilation of the gouge layers during the experiments suggests that water vaporization is relatively minor or negligible under impermeable conditions. On the other hand, natural slipping zones are likely to possess lower thermal conductivity (~1 W
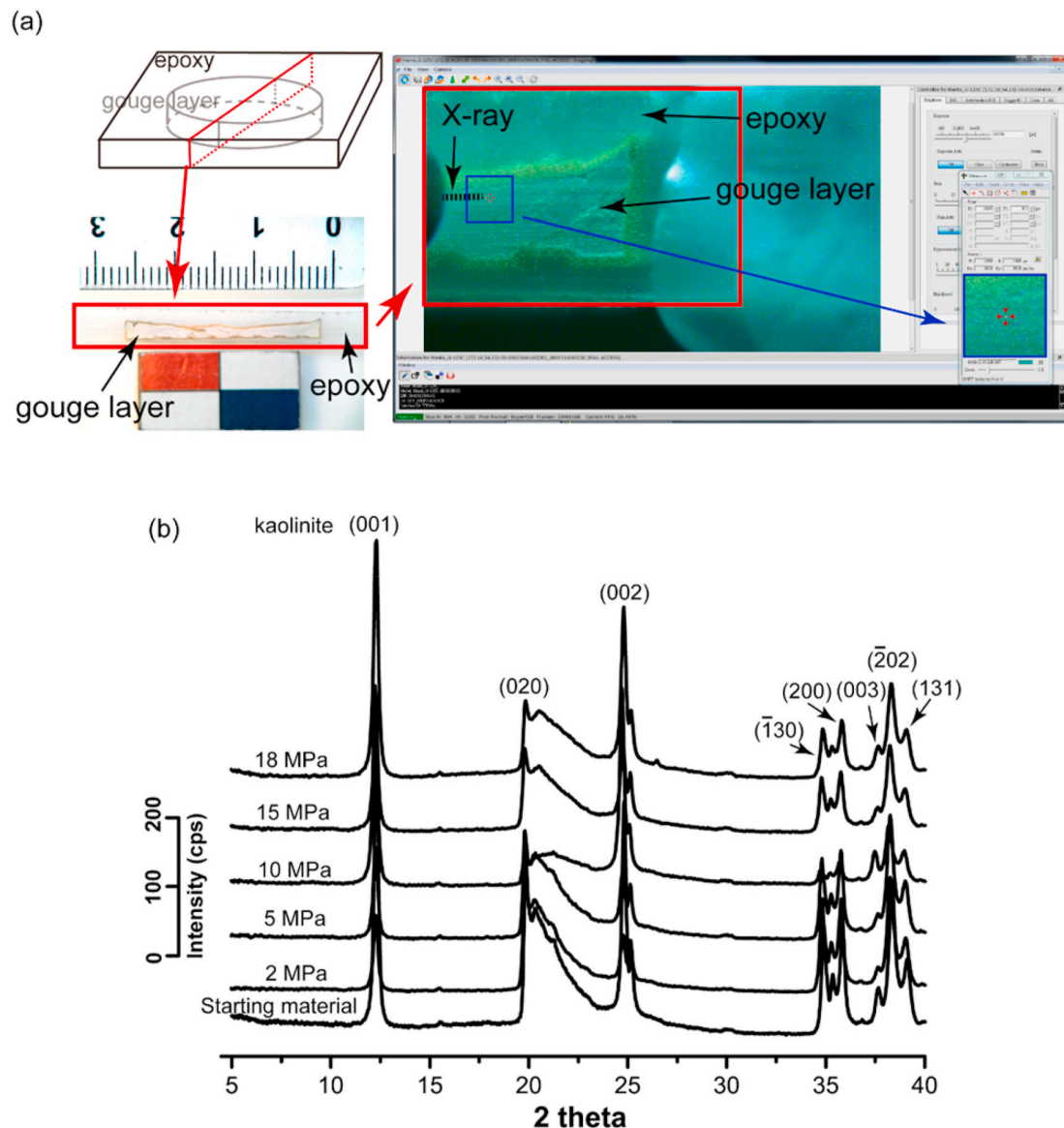
Fig. 9. In situ synchrotron X-ray analyses of a gouge layer. (a) The epoxyed gouge layer was cut into a slice (left panel of 11a). The slice of the epoxyed gouge layer was situated on the sample holder of synchrotron holder (right panel of 11a). The analyzed area of the sample can be selected via visual observation (the blue square in the bottom right corner). (b) Mineralogical phase of the selected area within the gouge layer. cps—counts per second. The peaks confirm that kaolinite is the only phase in all of the deformed gouge layers and the starting materials. (For interpretation of the references to color in this figure legend, the reader is referred to the Web version of this article.)

$m^{-1} K^{-1}$) and higher permeability (due to microfractures) than our impermeable metal sample holder (~40 W $m^{-1} K^{-1}$; Table 3). Thus, natural slipping zones may experience higher temperatures and lower pore pressures than in our experiments, possibly allowing water vaporization during seismic motion (Chen et al., 2017a, b).

4.4. Implications for frictional processes in nature

Natural slipping zones of shallow faults, subduction thrusts, and landslides are likely to contain water, and thus water-saturated clay gouge samples are relevant analogues for natural rock deformation. Numerous field observations show that gouge-bearing fault cores range from centimeters to several meters in width (e.g., Caine et al., 1996; Wibberley and Shimamoto, 2003; Faulkner et al., 2010). Field and seismological observations indicate that fault displacement at seismogenic depths can be localized within slipping zones a few centimeters thick (e.g., Ma et al., 2006; Wibberley and Shimamoto, 2003), and

microstructural studies demonstrate even more extreme localization of slip within gouge layers less than a few millimeters thick (e.g., Chester et al., 1993; Smith et al., 2011, 2013; Aretusini et al., 2019). This suggests that coseismic slip at depth can be extremely localized within clay-rich slipping zones that are embedded within fault cores (e.g., Sibson, 2003; Ma et al., 2006; Kuo et al., 2009, 2014a,b, 2015). Gouge-bearing fault cores are likely to have sufficiently low hydraulic diffusivity (i.e., impermeable condition) that they could trap pressurized fluids during coseismic slip at depth. This is also consistent with evidence for gouge fluidization observed in natural slipping zones (e.g., Boullier et al., 2009; Ujiie et al., 2007, 2008). For example, our resultant homogeneous texture within the gouge layer, a small temperature rise of hundreds of degrees and an estimated pore pressure of several megapascals during the experiments, can be comparable to the fluidization recorded in the ultracataclasite of the Mugi mélange, southwest Japan (Ujiie et al., 2007, 2008; Kameda et al., 2011).

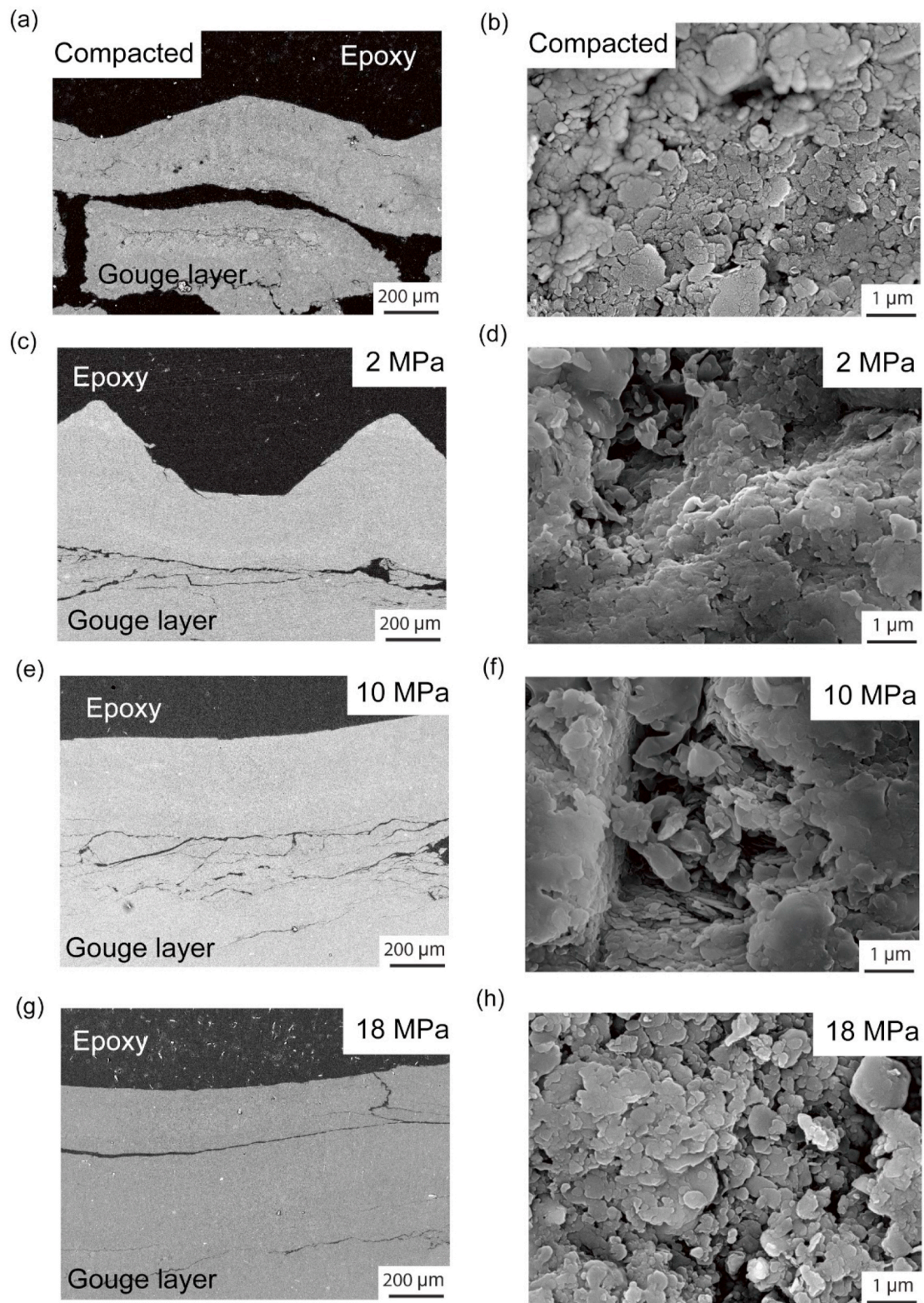On the other hand, the observations of core collected from the

Fig. 10. SEM images of water-saturated gouge layers from both compaction and shear experiments. (a, c, e, g) Petrographic thin sections of a radially cut gouge layer slices (with some scratches on the surface) and microstructures of both starting and deformed kaolinite samples at different normal stresses. Starting materials were compacted at 18 MPa. Triangular shapes on the top of gouge layer is as the consequence of compaction by the etched cylinder after the experiments. (b, d, f, h) Porous regions within a radially cut gouge layer slices and microstructures of both starting and deformed kaolinite samples at different normal stresses.
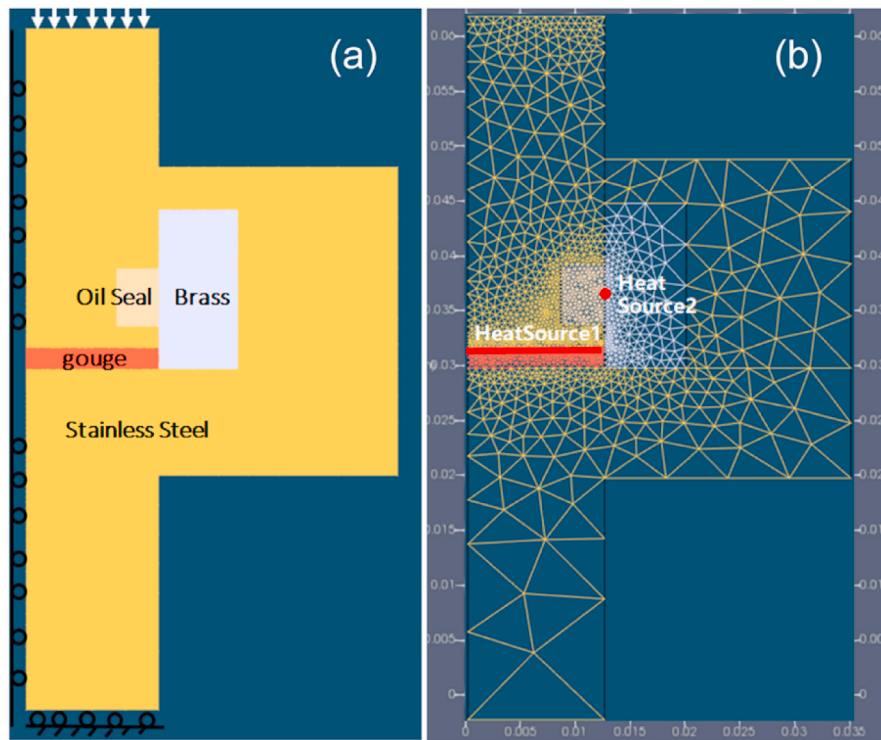
Fig. 11. Setup of 2D axisymmetric thermo-hydro-mechanical finite element model. (a) Geometry and material distribution for the model domain as well as the mechanical boundary settings. (b) Mesh and heat source distribution (right hand side).
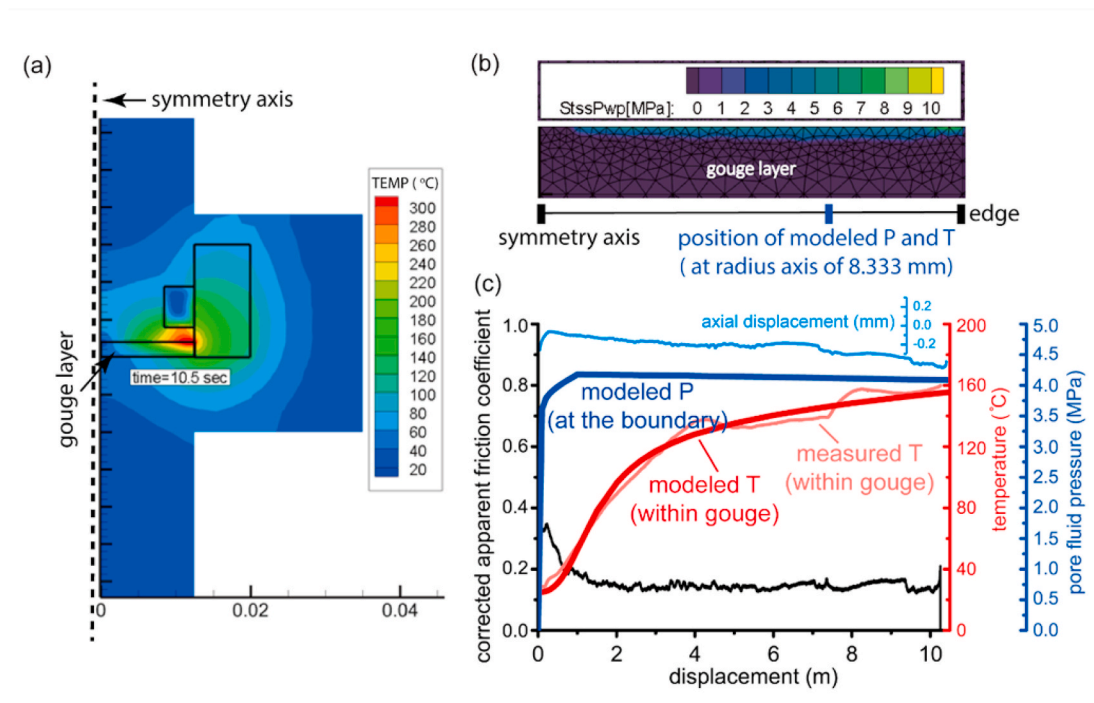

Fig. 12. Modeled evolution of pore fluid pressure (P) and temperature (T), and the T measured with a thermocouple during seismic slip (LHVR1223). (a) Temperature distribution within the gouge layer at the end of the modeling (10.5 s). (b) Pore fluid pressure distribution within the gouge layer at the end of the modeling (10.5 s). (c) Modeled evolution of both T and P at a radial position of 8.333 mm (the assumed position of the inserted thermocouple). Modeled T (in red color) is obtained in the middle of the gouge layer thickness, and modeled P is obtained at the contact boundary. Measured T (in pink color) is assumed to be in the middle of gouge layer. (For interpretation of the references to color in this figure legend, the reader is referred to the Web version of this article.)

Table 3
Flow and thermal properties of different materials used in the LVHR sample holder.

	Saturated hydraulic conductivity, [m/s]	Porosity	Density, [kg/m^3]	Specific heat, [J/kgK]	Thermal conductivity, [W/mK]
Stainless Steel	1.1E-23	0.0005	[a]8000	[a]500	[a]16
Gouge	[b]1.6E-13	0.3	[a]1231	[a]1269	[a]1.1
Oil Seal (Rubber)	1.7E-20	0.183	1200	2010	0.14
Brass	1.1E-23	0.001	[c]8710	[c]385	[c]60

Note: superscript a is from Aretusini et al. (2019); superscript b is from Crawford et al. (2008); superscript c is from Bossart (2005); the other values are the assumed values from references.

Taiwan Chelungpu fault Drilling Project (TCDP) show that the principal slip zone (PSZ) activated during the 1999 Mw 7.6 Chi-Chi earthquake was ~1–3 mm thick and surrounded by a ~1-m thick gouge-bearing fault core at a depth of 1111 m (Ma et al., 2006; Sone et al., 2007; Song et al., 2007; Kuo et al., 2014a). Boullier et al. (2009) presented a detailed microstructural analysis of the fault gouge from the PSZ, showing a random crystallographic grain orientation and an isotropic texture without clear evidence for shear bands or localization. Additionally, they observed a concentration of relatively large grains towards the top of the PSZ, and suggested that this microstructure formed as a result of the "Brazil nut" effect. They proposed that the PSZ experienced flash heating and thermal pressurization, with the gouge layers undergoing coseismic fluidization. In addition, estimated values of μ_{ss} from experiments conducted on PSZ gouges ranged from 0.18 to 0.5 (Sone et al., 2009; Mizoguchi et al., 2008), and estimated values of D_c were ~1–20 m (Sone et al., 2009; Tanikawa et al., 2009). Although the grain-size segregation and clay-clast aggregates observed in the Chi-Chi PSZ zone is lacking in the experimental products, the observed microstructures and measured experimental values are mostly consistent with our observations, supporting the interpretation that the Chi-Chi PSZ behaved as a fluidized layer due to thermal pressurization (or water vaporization; Chen et al., 2017b) under impermeable conditions during seismic slip.

Our experimental results, which are relevant to fluid-saturated and undrained conditions, suggest that fluidization of pore fluids is likely to be an important deformation process in deep-seated landslides (at depth > 100 m) and faults that contain low-permeability, gouge-bearing slipping zones. To summarize, our experimental data would be useful in understanding the frictional response associated with earthquake-rupture propagation within gouges at depth, consistent with natural and theoretical observation showing thinner gouge thicknesses with better efficiency for triggering thermal pressurization (Boullier et al., 2009; Noda and Shimamoto, 2005).

5. Conclusions

In this study, we developed a novel sample holder to deform fluid-saturated and clay-rich gouge samples at high-velocity and normal stresses up to 18 MPa. At a slip velocity of 1 m/s and normal stresses of 2–18 MPa, saturated kaolinite samples showed a dramatic friction drop from an apparent peak friction coefficient of c. 0.15 to a steady-state friction coefficient of c. 0.05. This was associated with progressive dilation of the gouge layers, and a measured and modeled bulk temperature increase of <160 C. A weak dependence of τ_{ss} on normal stresses suggests fluid-like mechanical behavior of the gouges. Microstructural and mineralogical analyses show random clay fabrics in all experiments, and no phase changes compared to the starting materials. Modeling of pore pressure and temperature suggests that pore fluids likely remained mainly in the liquid state. Overall, the mechanical, microstructural, and modeling data suggest that frictional weakening involves thermal pressurization and fluidization of the kaolinite gouges. Our results provide support to interpretations that some natural clay-rich slipping zones – for example fluidization records in the ultra-cataclasite of the Mugi mélange, southwest Japan, and the PSZ of the 1999 Mw 7.6 Chi-Chi earthquake – can be fluidized during coseismic deformation. Overall, our results indicate that pressurization and gouge fluidization may be important processes in low-permeability gouge zones, and that once frictional resistance is overcome, saturated gouge-bearing slip zones may provide little resistance to the propagation of large ruptures.

Author statement

L.-W.K conceived the present idea and coordinated the study; L.-W.K, W.-J.W, W.-T.L, W.-H.W conducted the experiments and analyzed the data; C.-W.K conducted modeling; L.-W.K, S.S co-wrote the manuscript with the input of C.-W.K; L.-W.K, Y.-H.H co-developed and tested the metal sample holder; all the authors participated in the interpretation of the data and in the discussion of the paper.

Declaration of competing interest

The authors declare that they have no known competing financial interests or personal relationships that could have appeared to influence the work reported in this paper.

References

Acosta, M., Passelègue, F.X., Schubnel, A., Violay, M., 2018. Dynamic weakening during earthquakes controlled by fluid thermodynamics. Nat. Commun. 9 (1), 3074. https://doi.org/10.1038/s41467-018-05603-9.

Alshibli, K., Akbas, I.S., 2007. Strain localization in clay: plane strain versus triaxial loading conditions. Geotech. Geol. Eng. 25, 45–55.

Aretusini, S., Plümper, O., Spagnuolo, E., Di Toro, G., 2019. Subseismic to seismic slip in smectite clay nanofoliation. J. Geophys. Res.: Solid Earth 124. https://doi.org/10.1029/2019JB017364.

Aretusini, S., Meneghini, F., Spagnuolo, E., et al., 2021. Fluid pressurisation and earthquake propagation in the Hikurangi subduction zone. Nat. Commun. 12, 2481. https://doi.org/10.1038/s41467-021-22805-w.

Bos, B., Peach, C.J., Spiers, C.J., 2000. Frictional-viscous flow of simulated fault gouge caused by the combined effects of phyllosilicates and pressure solution. Tectonophysics 327, 173–194.

Bossart, P., 2005. Characteristics of the Opalinus Clay at Mont Terri. http://www.mont-terri.ch/internet/mont-terri/en/home/geology/key_characteristics.html.

Boullier, A.M., Yeh, E.C., Boutareaud, S., Song, S.R., Tsai, C.H., 2009. Micro-scale anatomy of the 1999 Chi-Chi earthquake fault zone. G-cubed 10 (3), Q03016.

Boulton, C., Moore, D.E., Lockner, D.A., Toy, V.G., Townend, J., Sutherland, R., 2014. Frictional properties of exhumed fault gouges in DFDP-1 cores, Alpine Fault, New Zealand. Geophys. Res. Lett. 41, 356–362.

Boulton, C., Yao, L., Faulkner, D.R., Townend, J., Toy, V.G., Sutherland, R., Ma, S., Shimamoto, T., 2017. High-velocity frictional properties of Alpine Fault rocks: mechanical data, microstructural analysis, and implications for rupture propagation. J. Struct. Geol. 97, 71–92.

Brantut, N., Schubnel, A., Rouzaud, J.-N., Brunet, F., Shimamoto, T., 2008. High-velocity frictional properties of a clay-bearing fault gouge and implications for earthquake mechanics. J. Geophys. Res. 113, B10401. https://doi.org/10.1029/2007JB005551.

Brantut, N., Schubnel, A., Corvisier, J., Sarout, J., 2010. Thermochemical pressurization of faults during coseismic slip. J. Geophys. Res. 115, B05314. https://doi.org/10.1029/2009JB006533.

Brown, K.M., Kopf, A., Underwood, M.B., Weinberger, J.L., 2003. Compositional and fluid pressure controls on the state of stress on the Nankai subduction thrust: a weak plate boundary. Earth Planet Sci. Lett. 214, 589–603.

Caine, J.S., Evans, J.P., Forster, C.B., 1996. Fault zone architecture and permeability structure. Geology 24, 1025–1028.

Carpenter, B.M., Marone, C., Saffer, D.M., 2009. Frictional behavior of materials in the 3D SAFOD volume. Geophys. Res. Lett. L05302.

Carpenter, B.M., Marone, C., Saffer, D.M., 2011. Weakness of the San Andreas Fault revealed by samples from the active fault zone. Nat. Geosci. 4, 251–254.

Carpenter, B.M., Saffer, D.M., Marone, C., 2012. Frictional properties and sliding stability of the San Andreas fault from deep drill core. Geology 40 (8), 759–762.

Chen, J., Yang, X., Duan, Q., Shimamoto, T., Spiers, C.J., 2013. Importance of thermochemical pressurization in the dynamic weakening of the Longmenshan Fault during the 2008 Wenchuan earthquake: inferences from experiments and modeling. J. Geophys. Res. Solid Earth 118, 4145–4169.

Chen, J., Verberne, B.A., Spiers, C.J., 2015. Interseismic re-strengthening and stabilization of carbonate faults by "non-Dieterich" healing under hydrothermal conditions. Earth Planet Sci. Lett. 423, 1–12.

Chen, X., Elwood Madden, A.S., Reches, Z., 2017. The frictional strength of talc gouge in high-velocity shear experiments. J. Geophys. Res. Solid Earth 122, 3661–3676.

Chen, J., Niemeijer, A.R., Yao, L., Ma, S., 2017a. Water vaporization promotes coseismic fluid pressurization and buffers temperature rise. Geophys. Res. Lett. 44, 2177–2185. https://doi.org/10.1002/2016GL071932.

Chen, J., Niemeijer, A.R., Fokker, P.A., 2017b. Vaporization of fault water during seismic slip. J. Geophys. Res. Solid Earth 122, 4237–4276. https://doi.org/10.1002/2016JB013824.

Chester, F.M., Evans, J.P., Biegel, R.L., 1993. Internal structure and weakening mechanisms of the san andreas fault. J. Geophys. Res. Solid Earth 98, 771–786.

Chester, F.M., et al., 2013. Structure and composition of the plate-boundary slip zone for the 2011 Tohoku-Oki earthquake. Science 342, 1208–1211, 10 .1126/science.1243719.

Collettini, C., Niemeijer, A., Viti, C., Marone, C., 2009. Fault zone fabric and fault weakness. Nature 462, 907–910.

Collettini, C., Viti, C., Tesei, T., Mollo, S., 2013. Thermal decomposition along natural faults during earthquakes. Geology 41, 923–930.

Crawford, B.R., Faulkner, D.R., Rutter, E.H., 2008. Strength, porosity, and permeability development duringhydrostatic and shear loading of synthetic quartz-clay fault gouge. J. Geophys. Res. 113, B03207. https://doi.org/10.1029/2006JB004634.

De Paola, N., Hirose, T., Mitchell, T., Di Toro, G., Viti, C., Shimamoto, T., 2011. Fault lubrication and earthquake propagation in thermally unstable rocks. Geology 39 (1), 35–38.

Di Toro, G., Hirose, T., Nielsen, S., Pennacchioni, G., Shimamoto, T., 2006. Natural and experimental evidence of melt lubrication of faults during earthquakes. Science 331, 647–649. https://doi.org/10.1126/science.1121012.

Di Toro, G., Han, R., Hirose, T., De Paola, N., Nielsen, S., Mizoguchi, K., Ferri, F., Cocco, M., Shimamoto, T., 2011. Fault lubrication during earthquakes. Nature 471, 494–498.

Faulkner, D.R., Jackson, C.A.L., Lunn, R.J., Schlische, R.W., Shipton, Z.K., Wibberley, C. A.J., Withjack, M.O., 2010. A review of recent developments concerning the structure, mechanics and fluid flow properties of fault zones. J. Struct. Geol. 32 (11), 1557–1575.

Faulkner, D.R., Mitchell, T.M., Behnsen, J., Hirose, T., Shimamoto, T., 2011. Stuck in the mud? Earthquake nucleation and propagation through accretionary forearcs. Geophys. Res. Lett. 38, L18303.

Faulkner, D.R., Sanchez-Roa, C., Boulton, C., den Hartog, S.A.M., 2018. Pore-fluid pressure development in compacting fault gouge in theory, experiments, and nature. J. Geophys. Res.: Solid Earth 1–16.

Ferri, F., Di Toro, G., Hirose, T., Shimamoto, T., 2010. Evidence of thermal pressurization in high-velocity friction experiments on smectite-rich gouges. Terra. Nova 22 (5), 347–353.

Ferri, F., Di Toro, G., Hirose, T., Han, R., Noda, H., Shimamoto, T., Quaresimin, M., de Rossi, N., 2011. Low- to high-velocity frictional properties of the clay-rich gouges from the slipping zone of the 1963 Vaiont slide, northern Italy. J. Geophys. Res. Solid Earth 116, B09208.

Han, R., Shimamoto, T., Hirose, T., Ree, J.-H., Ando, J., 2007. Ultralow friction of carbonate faults caused by thermal decomposition. Science 316 (5826), 878–881. https://doi.org/10.1126/science.1139763.

Hirose, T., Shimamoto, T., 2005. Growth of molten zone as a mechanism of slip weakening of simulated faults in gabbro during frictional melting. J. Geophys. Res. Solid Earth 110, B05202.

Hunfeld, L.B., Chen, J., Niemeijer, A.R., Ma, S., Spiers, C.J., 2021. Seismic slip-pulse experiments simulate induced earthquake rupture in the Groningen gas field. Geophys. Res. Lett. 48, e2021GL092417 https://doi.org/10.1029/2021GL09241.

Hung, C.C., Kuo, L.W., Spagnuolo, E., Wang, C.C., Di Toro, G., Wu, W.J., Dong, J.J., Lin, W., Sheu, H.S., Yeh, E.C., Hsieh, P.S., 2019. Grain fragmentation and frictional melting during initial experimental deformation and implications for seismic slip at shallow depths. J. Geophys. Res. Solid Earth 124, 11150–11169.

Ikari, M.J., Saffer, D.M., Marone, C., 2009. Frictional and hydrologic properties of clay-rich fault gouge. J. Geophys. Res. Solid Earth 114, B05409.

Kameda, J., Ujiie, K., Yamaguchi, A., Kimura, G., 2011. Smectite to chlorite conversion by frictional heating along a subduction thrust. Earth Planet Sci. Lett. 305, 161–170.

Kitajima, H., Chester, J.S., Chester, F.M., Shimamoto, T., 2010. High-speed friction of disaggregated ultracataclasite in rotary shear: characterization of frictional heating, mechanical behavior, and microstructure evolution. J. Geophys. Res. 115 (B8), B08408.

Kuo, L.W., Song, S.R., Yeh, E.C., Chen, H.F., 2009. Clay mineral anomalies in the fault zone of the Chelungpu Fault, Taiwan, and their implications. Geophys. Res. Lett. 36, L18306.

Kuo, L.-W., Song, S.-R., Huang, L., Yeh, E.-C., Chen, H.-F., 2011. Temperature estimates of coseismic heating in clay-rich fault gouges, the Chelungpu fault zones, Taiwan. Tectonophysics 502, 315–327.

Kuo, L.-W., Hsiao, H.C., Song, S.-R., Sheu, H.S., Suppe, J., 2014a. Coseismic thickness of principal slip zone from the Taiwan Chelungpu fault Drilling Project-A (TCDP-A) and correlated fracture energy. Tectonophysics 619–620, 29–35. https://doi.org/10.1016/j.tecto.2013.07.006.

Kuo, L.-W., Li, H., Smith, S., Di Toro, G., Suppe, J., Song, SR., et al., 2014b. Gouge graphitization and dynamic fault weakening during the 2008 Mw 7.9 Wenchuan earthquake. Geology 42, 47–50. https://doi.org/10.1130/G34862.1.

Kuo, L.W., Song, Y.F., Yang, C.M., Song, S.R., Wang, C.C., Dong, J.J., Suppe, J., Shimamoto, T., 2015. Ultrafine spherical quartz formation during seismic fault slip: natural and experimental evidence and its implications. Tectonophysics 664, 98–108.

Lavallée, Y., Hirose, T., Kendric, J.E., De Angelis, S., Petrakova, L., Hornby, A.J., Dingwell, D.B., 2014. A frictional law for volcanic ash gouge. Earth Planet Sci. Lett. 400, 177–183.

Li, H., et al., 2013. Characteristics of the fault-related rocks, fault zones and the principal slip zone in the Wenchuan Earthquake Fault Scientific Drilling Hole-1 (WFSD-1). Tectonophysics 584, 23–42 doi: 10 .1016/j .tecto .2012 .08 .021.

Lin, H.-M., Wu, J.-H., Sunarya, E., 2018. Consolidated and undrained ring shear tests on the sliding surface of the hsien-du-Shan landslide in taiwan. Geofluids, 2018, Article ID 9410890, 12 pages, 2018. https://doi.org/10.1155/2018/9410890. Consolidated and Undrained Ring Shear Tests on the Sliding Surface of the Hsien-du-shan Landslide in Taiwan.

Lockner, D.A., Morrow, C., Moore, D., Hickman, S., 2011. Low strength of deep San Andreas fault gouge from SAFOD core. Nature 472, 82–86.

Logan, J.M., Rauenzahn, K.A., 1987. Frictional dependence of gouge mixtures of quartz and montmorillonite on velocity, composition and fabric. Tectonophysics 144, 87–108.

Ma, K.F., Tanaka, H., Song, S.R., Wang, C.Y., Hung, J.H., Tsai, Y.B., Mori, J., Song, Y.F., Yeh, E.C., Soh, W., Sone, H., Kuo, L.W., Wu, H.Y., 2006. Slip zone and energetics of a large earthquake from the taiwan Chelungpu-fault Drilling project. Nature 444, 473–476.

Mizoguchi, K., Hirose, T., Shimamoto, T., Fukuyama, E., 2007. Reconstruction of seismic faulting by high-velocity friction experiments: an example of the 1995 Kobe earthquake. Geophys. Res. Lett. 34, L01308.

Mizoguchi, K., Takahashi, M., Tanikawa, W., Masuda, K., Song, S.-R., Soh, W., 2008. Frictional strength of fault gouge in taiwan Chelungpu fault obtained from TCDP hole B. Tectonophysics 460 (1–4), 198–205.

Moore, D.E., Rymer, M.J., 2007. Talc-bearing serpentinite and the creeping section of the san andreas fault. Nature 448, 795–797.

Morrow, C.A., Moore, D.E., Lockner, D.A., 2000. The effect of mineral bond strength and adsorbed water on fault gouge frictional strength. Geophys. Res. Lett. 27 (6), 815–818.

Niemeijer, A.R., Collettini, C., 2014. Frictional properties of a low-angle normal fault under in situ conditions: thermally-activated velocity weakening. Pure Appl. Geophys. 171, 2641–2664.

Niemeijer, A.R., Spiers, C.J., Peach, C.J., 2008. Frictional behaviour of simulated quartz fault gouges under hydrothermal conditions: results from ultra-high strain rotary shear experiments. Tectonophysics 460 (1), 288–303.

Niemeijer, A., Di Toro, G., Griffith, W.A., Bistacchi, A., Smith, S.A.F., Nielsen, S., 2012. Inferring earthquake physics and chemistry using an integrated field and laboratory approach. J. Struct. Geol. 39, 2–36.

Noda, X., Shimamoto, T., 2005. Thermal pressurization and slip-weakening distance of a fault: an example of the Hanaore fault. Bull. Seismol. Soc. Am. 95, 1224–1233. https://doi.org/10.1785/0120040089.

Rempe, M., Di Toro, G., Mitchell, T.M., Smith, S.A.F., Hirose, T., Renner, J., 2020. Influence of effective stress and pore fluid pressure on fault strength and slip localization in carbonate slip zones. J. Geophys. Res.: Solid Earth 125, e2020JB019805. https://doi.org/10.1029/2020JB019805.

Rice, J., 2006. Heating and weakening of faults during earthquake slip. J. Geophys. Res. Solid Earth 111, B05311.

Sassa, K., Dang, K., He, B., Takara, K., Inoue, K., Nagai, O., 2014. "A new high-stress undrained ring-shear apparatus and its application to the 1792 Unzen–Mayuyama megaslide in Japan. Landslides 11 (5), 827–842.

Sawai, M., Shimamoto, T., Togo, T., 2012. Reduction in BET surface area of Nojima fault gouge with seismic slip and its implication for the fracture energy of earthquakes. J. Struct. Geol. 38, 117–138.

Schleicher, A.M., van der Pluijm, B.A., Warr, L.N., 2010. Nanocoatings of clay and creep of the san andreas fault at parkfield, California. Geology 38, 667–670.

Scholz, C.H., 2000. Evidence for a strong san andreas fault. Geology 28, 163–166.

Si, J., Li, H., Kuo, L.W., Pei, J., Song, S.R., Wang, H., 2014. Clay mineral anomalies in the Yingxiu–Beichuan fault zone from the WFSD-1 drilling core and its implication for the faulting mechanism during the 2008 Wenchuan earthquake (Mw 7.9). Tectonophysics 171–178, 619–620.

Si, J., Li, H., Kuo, L.W., Huang, J.R., Song, S.R., Pei, J., Wang, H., Song, L., Fang, J.N., Sheu, H.S., 2018. Carbonaceous materials in the longmenshan fault belt zone: 3. Records of seismic slip from the trench and implications for faulting mechanisms. Minerals 8 (457). https://doi.org/10.3390/min8100457.

Sibson, R.H., 2003. Thickness of the seismic slip zone. Bull. Seismol. Soc. Am. 93, 1169–1178.

Smith, S.A.F., Billi, A., Di Toro, G., Spiess, R., 2011. Principal slip zones in lime-stone: microstructural characterization and implications for the seismic cycle (Tre Monti Fault, Central Apennines, Italy). Pure Appl. Geophys. 168, 2365–2393.

Smith, S.A.F., Di Toro, G., Kim, S., Ree, J.H., Nielsen, S., Billi, A., Spiess, R., 2013. Co-seismic recrystallization during shallow earthquake slip. Geology41 63–66.

Sone, H., Shimamoto, T., 2009. Frictional resistance of faults during accelerating and decelerating earthquake slip. Nat. Geosci. 2 (10), 705–708.

Sone, H., Yeh, E.C., Nakaya, T., Hung, J.H., Ma, K.F., Wang, C.Y., Song, S.R., Shimamoto, T., 2007. Mesoscopic-structural observations of cores from the Chelungpu fault system, taiwan Chelungpu-fault Drilling project hole-A, taiwan, terr. Atmos. Ocean. Sci. 18 (2), 359–377. https://doi.org/10.3319/TAO.2007.18.2.359 (TCDP.

Song, S.R., Kuo, L.W., Yeh, E.C., Wang, C.Y., Hung, J.H., Ma, K.F., 2007. Characteristics of the litholgy, fault-related rocks and fault zone structures in the TCDP Hole-A. Terr. Atmos. Ocean Sci. 18, 243–269.

Spray, J.G., 2005. Evidence for melt lubrication during large earthquakes. Geophys. Res. Lett. 32, L07301. https://doi.org/10.1029/2004GL022293.

Takahashi, M., Mizoguchi, K., Kitamura, K., Masuda, K., 2007. Effects of clay content on the frictional strength and fluid transport property of faults. J. Geophys. Res. Solid Earth 112, B08206.

Tanikawa, W., Shimamoto, T., 2009. Frictional and transport properties of the Chelungpu fault from shallow borehole data and their correlation with seismic behavior during the 1999 Chi-Chi earthquake. J. Geophys. Res. 114, B01402. https://doi.org/10.1029/2008JB005750.

Tomasetta, I., Barletta, D., Poletto, M., 2013. The high temperature annular shear cell: a modified ring shear tester to measure the flow properties of powders at high temperature. Adv. Powder Technol. 24 (3), 609–617.

Tsutsumi, A., Shimamoto, T., 1997. High-velocity frictional properties of gabbro. Geophys. Res. Lett. 24 (6) https://doi.org/10.1029/97GL00503.

Ujiie, K., Tsutsumi, A., 2010. High-velocity frictional properties of clay-rich fault gouge in a megasplay fault zone, Nankai subduction zone, Geophys. Res. Lett. 37, L24310.

Ujiie, K., Yamaguchi, A., Kimura, G., Toh, S., 2007. Fluidization of granular material in a subduction thrust at seismogenic depths. Earth Planet Sci. Lett. 259 (Issues 3–4), 307–318.

Ujiie, K., Yamaguchi, A., Toh, S., 2008. Stretching of fluid inclusions in calcite as an indicator of frictional heating on faults. Geology 36 (2), 111–114. https://doi.org/10.1130/G24263A.1.

Ujiie, K., Tsutsumi, A., Kemeda, J., 2011. Reproduction of thermal pressurization and fluidization of clay-rich fault gouges by high-velocity friction experiments and implications for seismic slip in natural faults. In: Fagereng, Å., Toy, V.G., Rowland, J. V. (Eds.), Geology of the Earthquake Source: A Volume in Honour of Rick Sibson, vol. 359. Geological Society, London, Special Publications, pp. 267–285.

Vrolijk, P., van der Pluijm, B.A., 1999. Clay gouge. J. Struct. Geol. 21, 1039–1048.

Weatherley, D.K., Henley, R.W., 2013. Flash vaporization during earthquakes evidence by gold deposits. Nat. Geosci. 6, 294–298.

Wu, J.H., Wang, W.N., Chang, C.S., Wang, C.L., 2005. Effects of strength properties of discontinuities on the unstable lower slope in the Chiu-fen-erh-Shan landslide, Taiwan. Eng. Geol. 78, 173–186.

Wu, J.H., Liao, C.J., Lin, H.M., Fang, T.T., 2017. An experimental study to characterize the initiation of the seismic-induced Tsaoling rock avalanche. Eng. Geol. 217, 110–121.

Wu, W.J., Kuo, L.W., Ku, C.S., Chiang, C.Y., Sheu, H.S., Aprilniadi, T.D., Dong, J.J., 2020. Mixed-mode formation of amorphous materials in the creeping zone of the Chihshang Fault, Taiwan, and implications for deformation style. J. Geophys. Res. Solid Earth 125, 2020JB019862.

Yang, C.M., Yu, W.L., Dong, J.J., Kuo, C.Y., Shimamoto, T., Lee, C.T., Togo, T., Miyamoto, Y., 2014. Initiation, movement, and run-out of the giant Tsaoling landslide — what can we learn from a simple rigid block model and a velocity–displacement dependent friction law? Eng. Geol. 182, 158–181.

Yao, L., Ma, S., Chen, J., Shimamoto, T., He, H., 2018. Flash heating and local fluid pressurization lead to rapid weakening in water-saturated fault gouges. J. Geophys. Res. Solid Earth 123, 9084–9100.

Yeh, G.T., 1999. Computational Subsurface Hydrology Fluid Flows. Kluwer Academic Publishers.

Yeh, G.T., Burgos, B.D., Fang, Y., Zachara, J.M., 2000. Modeling biogeochemical kinetics: issues and data needs. XIII International Conference on Computational Methods in Water resources, 2000.

Yeh, G.T., Tsai, C.H., Jan, S.J., Kuo, C.W., Lai, S.H., Kuo, W.J., Li, M.H., 2017. HYDROGEOCHEM 4.1: A Coupled Model of Fluid Flow, Thermal Transport, and HYDROGEOCHEMical Transport through Saturated-Unsaturated Media - Version 4.1 (A Two-Dimensional Model). Taoyuan, Taiwan.